



Neural correlates of object identity and reward outcome in the sensory cortical-hippocampal hierarchy: coding of motivational information in perirhinal cortex

Julien Fiorilli ¹, Pietro Marchesi¹, Thijs Ruikes¹, Gerjan Huis in 't Veld¹, Rhys Buckton¹, Mariana D. Quintero¹, Ingrid Reiten², Jan G. Bjaalie ², Cyriel M.A. Pennartz^{1,*}

¹Systems and Cognitive Neuroscience Group, SILS Center for Neuroscience, University of Amsterdam, 1098 XH Amsterdam, The Netherlands,

²Institute of Basic Medical Sciences, University of Oslo, NO-0316 Oslo, Norway

*Corresponding author: Email: c.m.a.pennartz@uva.nl

Neural circuits support behavioral adaptations by integrating sensory and motor information with reward and error-driven learning signals, but it remains poorly understood how these signals are distributed across different levels of the corticohippocampal hierarchy. We trained rats on a multisensory object-recognition task and compared visual and tactile responses of simultaneously recorded neuronal ensembles in somatosensory cortex, secondary visual cortex, perirhinal cortex, and hippocampus. The sensory regions primarily represented unisensory information, whereas hippocampus was modulated by both vision and touch. Surprisingly, the sensory cortices and the hippocampus coded object-specific information, whereas the perirhinal cortex did not. Instead, perirhinal cortical neurons signaled trial outcome upon reward-based feedback. A majority of outcome-related perirhinal cells responded to a negative outcome (reward omission), whereas a minority of other cells coded positive outcome (reward delivery). Our results highlight a distributed neural coding of multisensory variables in the cortico-hippocampal hierarchy. Notably, the perirhinal cortex emerges as a crucial region for conveying motivational outcomes, whereas distinct functions related to object identity are observed in the sensory cortices and hippocampus.

Key words: multisensory; object recognition; visual cortex; barrel cortex; cross-modal.

Introduction

Object recognition serves animals to guide themselves to goals of interest, such as locations with food. Multisensory object representations are thought to be encoded by a hierarchically organized, cortical network in which unisensory information is initially processed in distributed unimodal regions and converges in higher order areas. The perirhinal cortex (PER) is often considered to be a central hub in this hierarchy, because of its reciprocal anatomical connections with, among others, the temporal association cortex, somatosensory whisker system, and visual cortex (Alvarez and Squire 1994; Murray and Bussey 1999; Eichenbaum 2000; Agster and Burwell 2009; Jacklin et al. 2016; Fiorilli et al. 2021). Lesion studies in rats that spontaneously explored their environment demonstrated that PER damage causes impairments in zero-delay recognition for objects having complex visual feature conjunctions and in cross-modal object recognition (Bartko et al. 2007; Albasser et al. 2015; Reid et al. 2012). As a first hypothesis to be considered here, it has been proposed that PER contributes to object (or item) perception in addition to memory (Dickerson and Eichenbaum 2010), especially when multiple object features or modalities have to be processed. Despite the lesion evidence, no electrophysiological studies have thus far

compared the influence of sensory inputs during object recognition between the PER, the sensory neocortical regions and hippocampus (HPC) of rodents.

A second hypothesis on the functionality of PER implies this structure in the coding of task and reward contingencies by interacting with interconnected structures involved in planning, motivation, and affect, such as the medial prefrontal cortex, orbitofrontal cortex, and amygdala (Agster et al. 2016; Kajiwara et al. 2003; Burwell et al. 1995; Fiorilli et al. 2021). Studies in monkeys showed that the PER carries information about cued reward schedules rather than the physical properties of sensory cues themselves, such as brightness (Liu and Richmond 2000; Eradath et al. 2015). In rats, PER neurons have been shown to code for spatial segments of a task environment (Bos et al. 2017), but also to represent behavioral choices on a fine time-scale during spatial responses on a touch screen (Ahn and Lee 2015). Spatial correlates in PER are generally not reported in the absence of spatial task constraints (e.g. when foraging in an open field arena; Burke et al. 2012; Deshmukh et al. 2012), suggesting that spatial-navigational correlates in PER may arise only when paired with reward prediction. Despite the available evidence for a contribution of PER to multisensory processing and value-based coding, it remains debatable whether sensory and value-based representations are

Received: May 24, 2023. Revised: December 21, 2023. Accepted: December 24, 2023

© The Author(s) 2024. Published by Oxford University Press.

This is an Open Access article distributed under the terms of the Creative Commons Attribution Non-Commercial License (<https://creativecommons.org/licenses/by-nc/4.0/>), which permits non-commercial re-use, distribution, and reproduction in any medium, provided the original work is properly cited. For commercial re-use, please contact journals.permissions@oup.com

both present in PER, and how PER compares to other regions in the cortico-hippocampal hierarchy.

The current study aimed to quantify sensory-evoked (tactile and visual) firing responses in the PER during multisensory object sampling, as well as firing-rate modulation by choice behavior and reward delivery. We additionally set out to compare these neural representations in PER to those simultaneously recorded from other regions of the cortico-hippocampal system. We devised a reward-driven multisensory object recognition task in which rats repeatedly discriminated between 2 familiar, solid 3D objects via whisker touch and/or vision. Object sampling enabled the rats to make a spatial choice to approach 1 of 2 goal locations, each of which was associated with one of the objects and yielded reward when correctly chosen. During this task, we simultaneously recorded ensemble activity with single-cell resolution from primary somatosensory barrel cortex (S1BF), secondary visual cortex (V2L), PER, and HPC (including CA1, CA3, and DG).

Our findings unveiled unique functional contributions of the PER in comparison to the sensory cortex and HPC. First, object representations were absent in PER even though neural ensembles S1BF, V2L, and HPC carried information about object identity. We additionally report a much higher sensitivity to tactile and visual inputs for HPC and the sensory cortical regions compared with PER. Second, representations in PER maximally differentiated between the choice sides (left vs. right) when rats kept their snout poked into 1 of 2 reward ports, indicating a specific role in coding of expected reward for a given goal location. Third, whereas modulations by trial outcome in V2L, S1BF, and HPC correlated to different post-reward behaviors (reward consumption vs. exiting the reward port), outcome-related responses in PER occurred earlier, viz. when rats started to sample for reward delivery by licking, and were mainly correlated with trial outcome (i.e. reward delivery or omission).

Population activity in both sensory cortices contained sensory-specific information on the object, whereas the HPC sustained modality-invariant representations of objects after reward consumption. In contrast, PER cells anticipated arrivals at a given goal location and represented unexpected trial outcome, suggesting a prominent contribution of PER in encoding motivational value of events, rather than a general role in object perception and recognition. These findings collectively reveal a dissociation within the cortico-hippocampal system, differentiating PER from the other recorded brain regions.

Materials and methods

Subjects

Data were collected from 4 28- to 44-wk-old male Lister Hooded rats (obtained from Envigo, The Netherlands). Rats were socially housed under a reversed day/night cycle (lights off: 8:00 AM, lights on: 8:00 PM) and food restricted to maintain their body weight at 85% of the ad libitum growth curves of Harlan, taking [Rolls and Rowe \(1979\)](#) as a reference. All experiments were performed in accordance with the National Guidelines on Animal Experiments and were approved by the Animal Experimentation Committee of the University of Amsterdam.

Apparatus

Behavioral training was performed in a darkened room on an elevated T-shaped platform (30W × 35L × H60 cm, 60 cm from floor) with a reward well for sucrose solution (15%) delivery at opposed sides (30 cm distance; [Fig. 1a](#)). The training apparatus was fully

automated with custom-written MATLAB code on a Windows PC, and hardware was controlled through a Field Programmable Gate Array and an Arduino. A pneumatic door prevented access to the objects during the intertrial interval (ITI). Nose pokes into reward ports (4W × 4H cm) and lick events were detected by 2 different IR phototransistors in each reward port ([Fig. S2e](#)). Reward was delivered upon nose poke entry by a syringe pump (Razel, USA). The on- and offset of the object sampling epoch were estimated during the task by phototransistors in front of the object, but more precisely defined for analysis afterwards by means of video tracking. The 2 reward ports were located on either side of the sampling platform, facing each other at a distance of 30 cm. To analyze object-sampling behavior, an infrared high-speed camera was mounted 40 cm above the rat's head (500 frames/s; M3 Camera from Integrated Design Tools, USA, with 50 mm/F0.95 lens, Navitar, USA; Using MotionStudio software, Integrated Design Tools, USA). Object sampling, detected with phototransistors and infrared beams, triggered the high-speed camera to write 900 video frames for 1.8 s to the PC. Background illumination of diffuse IR light was reflected from 5 LED arrays (Sygonix, 310 mA, wavelength: 850 nm) to the camera by a mirror located underneath the sampling region. White semitransparent Perspex acrylic was used to diffuse the IR light coming from the side before being reflected to the camera. A second infrared camera (SONY EVI-D100P), placed 150 cm above the platform, allowed the experimenter to monitor the animal's overall behavior on the elevated platform. A single IR light (Sygonix, 310 mA, wavelength: 850 nm) mounted 40 cm above the platform weakly illuminated the maze for recording images on this camera.

The 3D objects consisted of plastic LEGO configurations, which were mounted on black H11 × W20 cm rectangular acrylic background sheets with hot melt adhesive. Objects were randomly presented using a rotating stepper motor at the start of each ITI. The objects were randomly rotated before bringing the objects into place for an upcoming trial, in order to prevent that sounds related to stepper motor rotations would enable the animal to predict the upcoming object and associated reward location. In visual and multisensory trials, an object-focused white LED light was triggered upon object sampling. In tactile and multisensory trials, the objects were presented at a gap distance of 15 to 16 cm away from the elevated platform, which limited object contact to whiskers only (at this distance the object was typically at a distance of 0.5 to 3.5 cm from the snout during tactile sampling, see also [Harris et al. 1999](#)). In visual trials and catch trials, objects were presented further away (22 to 23 cm from platform), which made it impossible for the rat to reach the object with its whiskers. Tactile object sampling was thus controlled by the gap distance to the object, and visual sampling was controlled by light illumination in an otherwise dark room. Computers, acquisition systems, and experimenter were situated in a separate room from the darkened experimental room to prevent light leakage.

Behavioral procedure

We recorded 4 male Lister Hooded rats that were trained on a 2-alternative forced-choice object discrimination task. To correctly perform a trial, rats had to sample 1 of 2 possible objects, retract from the object-sampling port, and subsequently make a choice by nose-poking into 1 of 2 reward ports, placed on the left and right side of the object-sampling port ([Fig. 1](#)). The object-side associations were counterbalanced over the 4 rats, but the objects remained unaltered. A trial started after an ITI of 12 s, after which a pneumatic door opened ([Fig. 1a](#)) and access to the object became possible. The door closed when the rat initiated a nose

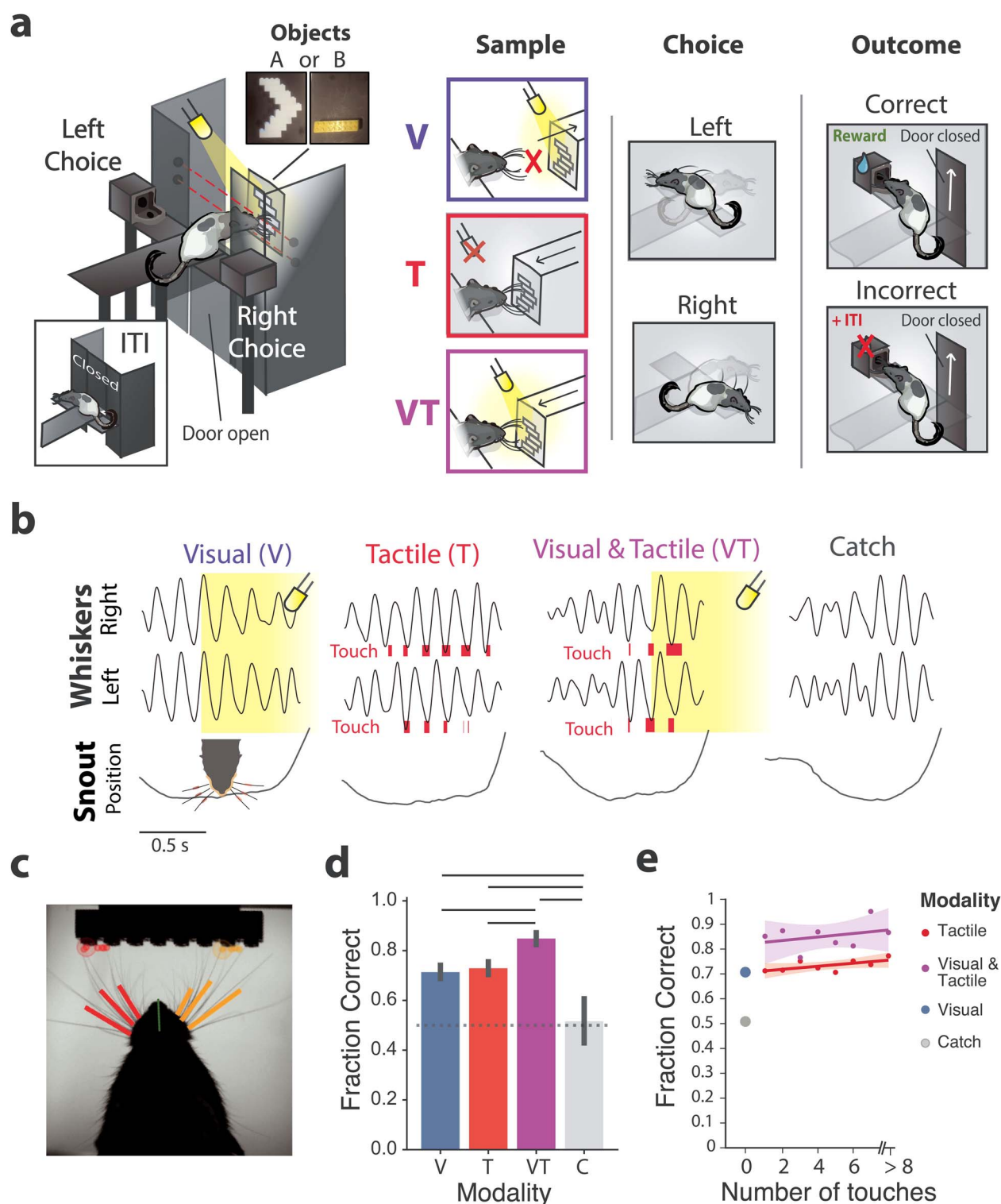


Fig. 1. Performance and single trial examples of the multisensory object discrimination task. **a)** Schematic overview of the reward-driven discrimination task. Rats were trained to associate 2 objects with opposed reward sides. Different trial types were presented randomly within a session and allowed object sampling either by vision (V), touch (T), or by both senses combined (VT). **b)** Example trials with object approach and time course of whisking behavior. Rats started whisking during the approach toward the object. In tactile and multisensory trials, rats could reach and palpate the object with its whiskers. In visual and multisensory trials, an LED light illuminated the object when the snout was in front of the object. The lower row displays the snout distance from the object over time, during the approach to and withdrawal from the object. Touch epochs are indicated in red and illumination in yellow. **c)** Example frame taken from a high-speed video during tactile object sampling, with overlaid whisker and snout tracking. **d)** Rats performed the task above chance-level in all trial types, taking the catch trials with no object information (neither visual nor tactile) as the chance-level comparison. Performance in multisensory trials was significantly higher than in visual and tactile trials ($P < 0.05$, 1-way ANOVA [$F = 31.376$, $P < 0.000$] with post hoc Tukey test). Bars indicate 95% CIs. **e)** Task performance over amount of touches during object sampling. Multisensory sampling improved task performance regardless of the number of touch epochs. This indicates that the increased performance in multisensory trials is not the result of a more elaborate tactile sampling strategy in the presence of light. Lines are linear fits and shaded areas indicate the 95% CI.

poke in one of the reward ports. The modality (visual, tactile, or multisensory) was selected randomly per trial, but was repeated after an incorrect response to discourage any preferred modality bias during a session. Rats were implanted and recorded when they reached a stable performance of at least 70% correct for each trial type during 7 consecutive days.

Surgical procedures and electrophysiology

Recording areas were targeted in the right hemisphere with a custom-built microdrive that contained 36 individually movable tetrodes (Nichrome wire, California Fine Wire, diameter: 13 μm , gold-plated to an impedance 300 to 800 $\text{k}\Omega$ at 1 kHz), 4 of which were used as reference (Lansink et al. 2007; Bos et al. 2017). For 2 out of 4 rats, tetrodes were collected in 4 bundles, each of which targeted toward PER, dorsal HPC (CA1, CA3, and DG), V2, and S1BF (PER area 35/36; coordinates: -6.0 AP, 6.5 DV, 7.0 ML; dorsal CA1 and CA3 coordinates: -3.48 AP, 2.0 ML, 2.5 DV; V2L coordinates: -6.0 AP, 2.8 DV, 5.8 ML; and S1BF coordinates: -3.0 AP, 5.0 ML, 2.8 DV). For the other 2 rats, the HPC bundle was omitted; tetrodes from this bundle were appended to the V2L and PER bundles. Rats received preoperative, subcutaneous injections of the analgesics buprenorphine (Buprecare, 0.04 mg kg^{-1}) and meloxicam (Metacam, 2 mg kg^{-1}) as well as the antibiotic enrofloxacin (Baytril, 5 mg kg^{-1}). Anesthesia was induced with 3.0% isoflurane, and was kept on 1.0% to 2.0% isoflurane during surgery. A heating pad was used to maintain body temperature. Lidocaine was applied directly on the periosteum for additional, local analgesia before exposing the skull. The skull surface was thoroughly cleaned with 3% hydrogen peroxide solution, and washed thrice with saline. Six screws, from which one served as ground (occipital bone), were inserted in the skull to improve the stability of the implant. After craniotomy and durotomy were performed, the drive was positioned using a stereotaxic holder. The craniotomy was then sealed using silicone adhesive (Kwik-Sil), and dental cement (Kerr-total adhesive Opti-bond Solo Plus and 3 M Unitek Transbond) was applied to anchor the drive on the skull and screws (Lansink et al. 2007; Bos et al. 2017). Postoperative care included a subcutaneous injection of meloxicam on the 2 days following surgery, and Baytril 1 day after surgery. From the 3rd day after surgery, tetrodes were gradually lowered toward their target regions on a daily basis. Recording locations were estimated based on the number of turns to the tetrode guiding screws, and by assessing the Local Field Potential, sharp wave ripples in CA1 and CA3, and spike signals during signal acquisition.

Neurophysiological signals were continuously acquired at a sampling rate of 32 kHz with a Digital Lynx SX 144 channel system (Bozeman, MT) and high pass filtered at 0.1 Hz. The signals were pre-amplified with a headstage before being fed through an automated commutator (Neuralynx). Spike detection and sorting were performed offline using Klusta and manually curated using Phy GUI (Rossant et al. 2016, also for optimized spike detection and clustering parameters). Clusters were included as units based on their spike waveforms, autocorrelation and stability over time. A unit was considered a single-unit if $<0.5\%$ of its spikes occurred in the refractory period (1.2 ms) and its isolation distance to other spike clusters was above 5. Only cells with an average firing rate higher than 0.5 Hz during trials (8 s pre- to 5 s post-poke for reward) were included in single-unit analysis. Units that passed the above-mentioned criteria, but no other cases, were considered single units in the analysis. Spiking activity was aligned to events of interest and then convolved using an Alpha kernel ($\sigma = 100$ ms, $\text{step} = 10$ ms), unless specified differently.

Histology and anatomic registration of tetrode locations

On the final recording day, electrolytic lesions were made at the tip of each tetrode by passing current (18 μA for 2 s) through 2 leads of each tetrode. Approximately 24 h after lesioning, animals were deeply anesthetized with Nembutal (sodium pentobarbital, 60 mg ml^{-1} , 1.0 mL intraperitoneal; Ceva Sante Animale, Maassluis, the Netherlands) and transcardially perfused with a 0.9% NaCl solution, followed by a 4% paraformaldehyde solution (pH 7.4, phosphate-buffered). After postfixation, transversal sections of 40 to 50 μm were cut using a vibratome or sliding microtome and stained with Cresyl Violet to reconstruct tetrode tracks and localize their end-points. To allow direct comparison of recording regions between rats, we extracted spatial coordinates for all tetrode locations after registering the histological section images to the Waxholm Space Atlas of the Sprague Dawley rat Brain v3 (Research Resource Identifier [RRID]: SCR_017124; Papp et al. 2014; Bjerke et al. 2018) using the QuickNII software (RRID: SCR_016854; Puchades et al. 2019).

Video tracking

We tracked whisker touches, snout, and global position of the whisker array at either side of the snout, by training DeepLabCut (DLC; Mathis et al. 2018) on 548 video frames originating from 15 different sessions ($n=4$ rats). Video frames for manual annotations of head and whisker positions were picked from different sessions by k-means clustering based on frame appearances (Mathis et al. 2018). This ensured that labeling was performed on frames that looked different. We additionally hand-picked 260 frames from sessions that varied in snout position, sharpness, illumination, and magnification. For quantification of whisking behavior, we tracked the rostral, caudal, and mid-line of the whisker array at either side of the snout. We verified the tracking accuracy by (i) computing the median distance between tracked point and real annotated point (Mathis et al. 2018), (ii) plotting the whisker angles, head angles, and moments of touch, and verifying that these followed the expected rhythmicity and spatial dimensions (rats whisk/palpatate at a frequency of ~ 8 to 20 Hz; Berg and Kleinfeld 2003; Mitchinson et al. 2007; Sachdev et al. 2003), and (iii) visually inspecting videos with overlaid tracked whisker angles, tracked snout, and tracked touches (S2a to c, SI Video). Because the timing of individual whisk touches was especially important to us, we additionally manually labeled all individual video frames from 5 sessions as having a whisker touch in it or not. Comparisons between DLC-based whisk touches and manual whisk touches revealed a high degree of overlap (Fig. S2d).

Lick-rate analysis

To quantify the behavioral changes occurring in response to reward delivery, we computed a separate lick-PETH for rewarded and unrewarded nose pokes into the reward port (Fig. 9a). Based on this licking behavior, we identified an epoch in which rats had started to sample for the reward in 95% of the trials (measured by means of the first lick after nose poke entry). We identified this epoch as the "Initial Outcome Period" (IOP), because rats started to exit the nose poke site upon omitted reward delivery only after this point. Thus, significant outcome coefficients later than this epoch could also be explained by behavioral changes in lick patterns and poke behavior following reward sampling, whereas modulations within this epoch could not.

Light and touch onset modulation indices

We quantified responses to light onsets by comparing average firing rates during object sampling between visual, tactile, and multisensory trials. Here, we restricted the analysis to a response window of 200 ms after the start of object sampling, thereby including the light and tactile onsets and limiting influences related to retraction movements. For every neuron, we used the area under the receiver operating characteristic curve (AUROC) to measure if sensory onsets from a given modality evoked higher firing rates compared with when this input was absent (e.g. for light onset responses we asked if $VT > T$ and if $V > T$). Statistical significance of sensory differentiation was assessed by 1000 permutations of the trial modality labels to obtain a distribution of surrogate indices. AUROC values were considered to be significant for the tested modality when they fell above the one-sided 95% confidence interval (CI) of the surrogate distribution and the corresponding neurons were then considered to be modulated by the tested modality (see Fig. 3a for an example of visual modulation). For all cells that were significantly responsive to light onset, we additionally quantified tactile modulations of the light onset responses by contrasting visual responses with combined touch (VT) to visual responses in absence of touch (V). A cell was considered to be suppressed or enhanced when its AUROC values fell, respectively, below or above the 2-sided 95% CI of the surrogate distribution.

Responses to touch were quantified similarly as for light onset, but AUROC values were now computed based on the average firing rates within the full tactile sampling epoch in a given trial (from the first touch to the last touch; Figs. 1a and 4a). Tactile trials with <3 touches were excluded from the analysis.

To quantify very transient touch onset modulations, we identified clearly defined whisker touches of relatively long durations (of both left and right whiskers combined). This was achieved by selecting touch onsets for which at least 60% of the frames in the subsequent 50 ms contained a touch. Additionally, touch onsets were required to have a 50 ms pre-touch period with at most 30% of video frames displaying a touch. We selected sessions in which this procedure identified at least 30 touch onsets. For every neuron, we next binned spikes in the 50 ms before each touch onset (pre-touch) and after each touch onset (post-touch, Fig. 4d). The touch-onset modulation (TOM) index consisted of the AUROC values of pre-touch vs. post-touch spikes. We then randomly permuted the pre-touch and post-touch labels 100 times per-touch, and recomputed the AUROC values to obtain the null distribution. TOM index values were considered significant when they fell outside the 95% confidence of the surrogate distribution.

Object coding

For every neuron, firing rates were aligned to the start of sampling and convolved as described earlier (see Surgical Procedures and Electrophysiology). A GLM (see below) was used to disentangle the contribution of choice side and object identity, separately for visual and tactile trials. We restricted the significance estimation to the first 0.5 s after the start of sampling as we assumed that correlates of object identity would emerge during, or shortly after object sampling and recognition measured by means of whisker and snout tracking (for the object encoding over time, see Fig. 5d). We additionally verified that cells with significant object predictors also tended to have higher AUROC values for the object identity compared with the choice side, computed over the average firing rates from our analysis time window (see Results).

Population decoding

Because multiple units can contribute to a population code, we included all manually curated units including those that did not meet the criteria for single-units in the population decoding analysis (N units: S1BF = 203, V2L = 488, PER = 257, HPC = 307). Spikes were grouped in 300 ms time bins, advanced with increments of 10 ms.

In the object decoding analysis within trial types, a random forest classifier with 200 trees was trained to identify the object within every unique combination of modality and choice side. This was achieved by randomly selecting 3 trials with the same choice side within a particular sensory modality. The accuracy of classification was then evaluated over time using 3×3 cross-validated predictions. We then computed the average classification accuracies for both choice sides within a modality. This process allowed us to derive an object population decoding accuracy within a specific modality while mitigating the influence of the choice side at each time point. To account for variability, this entire procedure was iterated 100 times, each time randomly selecting trials and cells. Significance was assessed using 95% CIs derived from decoding inaccuracies based on shuffled distributions.

Decoding of trial type (Fig. 6) was performed by randomly drawing 2 trials for each combination of sensory modality, choice side, and object identity out of each recording session, which resulted in a total of 8 trial categories to classify (one example of them being the tactile trials in which the rat sampled object A, and chose the left reward port). Hundred cells were randomly selected across all sessions available from all subjects. At each time bin, we decoded the trial type from spiking activity of the selected cells with a random forest classifier with 200 trees. To prevent overfitting, we restricted each tree to maximally 4 splits, and used a 3×3 cross-validation routine (Bos et al. 2019; Glaser et al. 2020). This entire procedure was repeated 100 times, each time randomly drawing trials and cells. Prediction accuracy for a given trial type was scored within each trial subcategory using a contingency matrix. For instance, the decoding accuracy for the choice side was computed across all left and right choice trials (Fig. 6d). Significance was assessed using 95% CIs derived from decoding inaccuracies based on shuffled distributions. Object population decoding across sensory modalities (Fig. 7) was performed as described above, except that the classifier was trained on only the neural activity derived from tactile trials. Subsequently, we examined the decoder's ability to generalize across sensory modalities by classifying objects based on neural activity from the visual trials.

The pseudo-population decoding of left and right choice (Fig. 8) based on linearly warped firing rates was performed similarly, but now by randomly drawing 10 left tactile or visual and 10 right tactile or visual trials out of each recording session (recording sessions with fewer than 10 trials per type were excluded). For selected cells and trials, firing rates were linearly warped to align the moments of retraction and reward-site pokes to the median event times computed across all sessions (median times were computed separately for visual and tactile trials). The number of splits per tree was not restricted for this analysis because overfitting was less of a concern given the higher number of trials across only 2 categories.

Generalized linear model

During object sampling or reward consumption, multiple variables may affect firing rates of individual cells. To disentangle

the contribution of photic condition, choice (Left/Right), reward, and object identity, we examined the linear relation between each of these task variables and the neural responses with a generalized linear model (GLM; *Statsmodels* toolbox). We used a Poisson regression to approximate firing rate statistics (Fig. S5b). Single-unit activity was aligned to the event of interest (start sample or nose poke for reward, NPR) and convolved as described earlier. The GLM was fitted to describe the relationship between the binary trial variables and single-unit firing rate distributions independently on each time point. Accuracy of the GLM model was scored by predicting the firing rates of each cell for all trials on each time point, based on the coefficients through cross-validation, and by calculating the proportion of explained variance (R^2 score) between predicted and actual firing rates (1.0 being the highest possible score). We verified the accuracy of the model fit by comparing R^2 scores of time bins that had at least one significant predictor to time bins without any significant predictor contribution, as well as to time bins from a baseline epoch (−8 to −3 s before the poke), or by comparison to chance-level accuracies obtained by randomly permuting trial labels independently at each time-bin 500 times (Fig. S5). Statistical significance of a predictor at a given time point was determined with Z-statistics by comparing the explained variance against a model fit in which the tested predictor had no relation to the firing rates. P-values over time for a given cell were corrected by the Benjamini–Hochberg procedure.

Statistical significance of proportions of neurons

Statistical significance of cell proportions was determined according to z-test for proportions:

$$Z = \frac{\hat{p} - p_0}{\sqrt{\frac{p_0(1-p_0)}{n}}}$$

Where \hat{p} is the observed proportion of significant cells during an epoch of interest, and p_0 the proportion of significant cells during chance level distributions, n is the total number of cells.

Results

Behavioral results and multi-area electrophysiology

We trained freely behaving rats ($n=4$) on a multisensory 2-object recognition task, in which solid objects had to be associated with different choice sides in order to obtain reward. During a given trial, object sampling was either possible by whisker palpation, vision, or by both senses combined (Fig. 1a). After an ITI (12 s), rats could sample an object, located a gap distance away from the elevated platform. Whisker palpation was prevented in visual trials by having a larger gap distance to the object, and availability of visual object information was controlled with an object-focused illumination in an otherwise darkened room. This illumination was triggered when rats perched across the gap and toward the object, forcing a similar pose and head-position across the different trial types. Rats whisked in the air during all trials (Fig. 1b and c; SI: Video), also when no tactile information was available. The rats subsequently retracted their body from the object-sampling port and turned to make a left or right nose poke, where the correct choice depended on object identity. Pokes on the correct object-associated side were rewarded with sucrose delivery. An incorrect response led to an extended ITI (20 s)

without reward delivery. To verify that rats could not use odors or sounds related to the automated object-presentation mechanism, we also introduced catch trials. During these catch trials the object-presentation mechanism remained active so that objects were rotated into place for future presentation during the ITI, but illumination was kept off and the object itself was out of whisker reach. Rats were expected to perform around chance level for these catch trials if they based their decision solely on visual or tactile information. Rats learned to discriminate between objects with an above-chance accuracy in all trial types, except for catch trials (Fig. 1d; visual trials: $T(27) = 14.80$, $P < 0.001$, tactile trials: $T(27) = 16.33$, $P \leq 0.001$, multisensory trials: $T(27) = 26.93$, $P < 0.001$, and catch trials: $T(27) = 0.34$, $P = 1.00$, 1-sample t-test, Bonferroni corrected). Discrimination performance was significantly higher in multisensory than unisensory trials, indicating that rats used both visual and somatosensory information to guide their decisions (Fig. 1d; multisensory vs. visual trials: $P = 0.001$; multisensory vs. tactile trials: $P = 0.034$; 1-way ANOVA [$F = 31.37$, $P < 0.001$] with post hoc Tukey test). Multisensory sampling improved task performance regardless of the number of touches (Fig. 1e).

We simultaneously recorded the activity of neuronal ensembles in multiple regions along the cortico-hippocampal hierarchy during 27 sessions from 4 well-trained rats. Each animal was chronically implanted with a quadrigate that contained 36 tetrodes enabling simultaneous recording of single units from S1BF ($n=91$), V2L ($n=279$), and PER ($n=191$, areas 35/36, central-caudal region; Fig. 2 and Table S1; Bos et al. 2017; Vinck et al. 2016). In 2 of these animals, we additionally recorded from the dorsal HPC ($n=179$; subfields: CA1=59, CA3=88, DG=32). Units in the HPC were pooled across subfields for analysis, unless specified differently.

Tactile and visual stimulation during object sampling evokes neural activity in sensory cortices and HPC, but not in PER

The PER is thought to be richly supplied with object information from the different sensory cortices. We initially asked whether PER neurons preferentially discharge during object sampling regardless of the sensory modality, as predicted by the hypothesis that PER primarily subserves object perception. We subdivided behavioral trials into an object sampling phase, a choice phase (marked by locomotion away from the sampling port and left vs. right turn), and a trial outcome phase initiated by an NPR. The sampling period is marked by the initiation of object sampling up to the start of locomotion toward the reward ports (defined by means of high-speed video tracking). Because of the self-paced nature of the task, these task phases had variable durations. We therefore aligned the neural data by linearly warping the firing rates between the start of sampling, the choice-initiation moment (defined as the moment of retraction from the object), and the time of the NPR. We found no preferential firing during object sampling in PER (peak firing rate probability tested against chance level of uniformly distributed events, PER probability: 0.067, $Z = -3.06$, $P = 3.995$, proportions z-test, Bonferroni corrected; Figs. 2c and d and S3). Instead, PER cells preferentially discharged following the NPR (PER probability: 0.294, $Z = 9.79$, $P < 0.001$, proportions z-test, Bonferroni corrected; Figs. 2c and e and S3). In contrast, most cells in sensory regions S1BF and V2L discharged most strongly during the choice phase (S1BF probability: 0.40, $Z = 5.65$, $P < 0.001$; V2L probability: 0.39, $Z = 9.79$, $P < 0.001$, proportions z-test, Bonferroni corrected).

Under our first hypothesis, holding that the PER contributes to complex perception by integrating multimodal object information

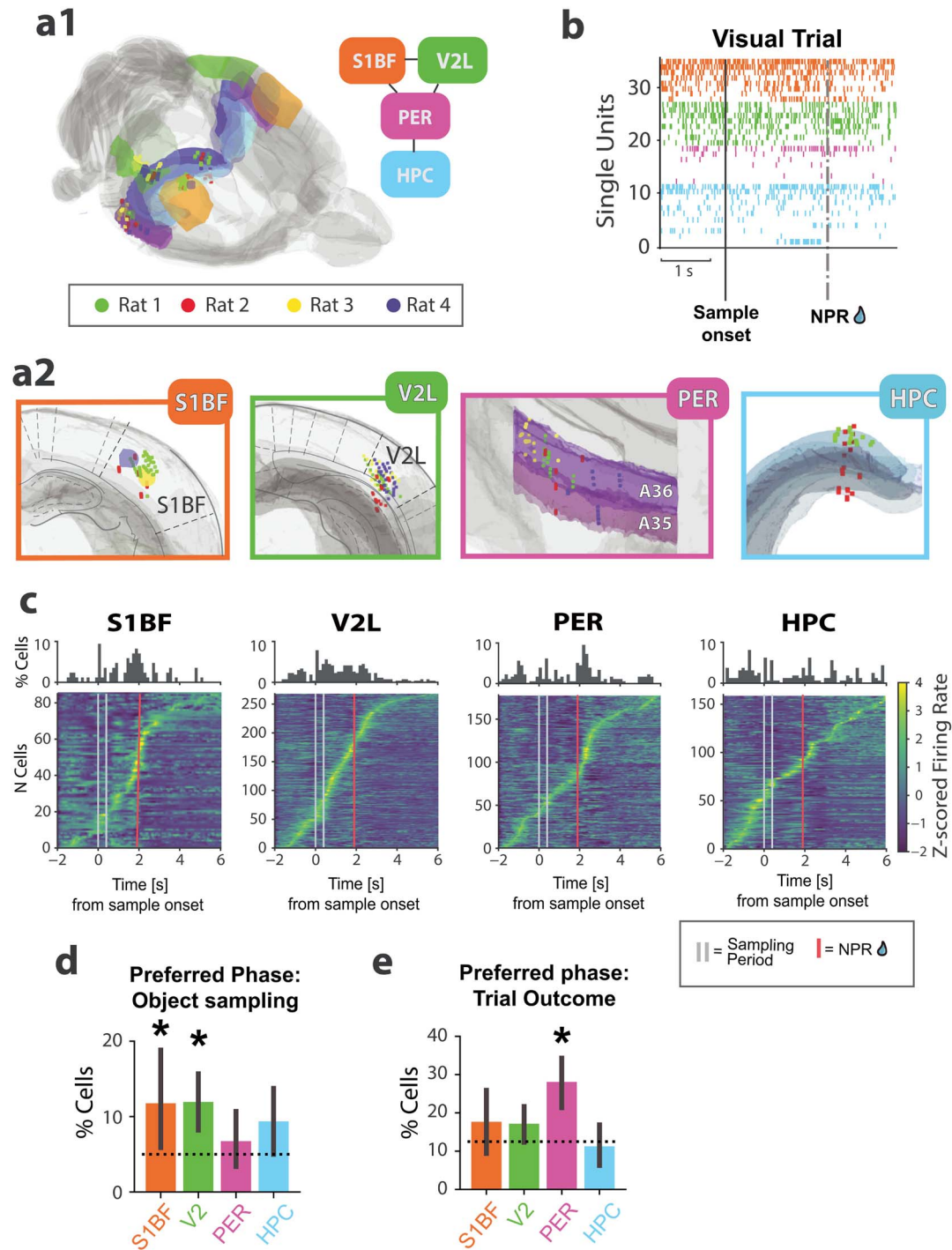


Fig. 2. Simultaneous multi-area ensemble recordings from the cortico-hippocampal hierarchy during the object recognition and outcome phases of the task. a1 to 2) 3D spatial registration of tetrode recording locations. a1) Overview of all recording locations mapped on the Waxholm space atlas, color-coded per rat. Top-right schematic inset depicts the crude anatomical organization of the 4 recorded areas situated along the cortico-hippocampal hierarchy. a2) Close-up views of target regions S1BF, V2L, PER, and HPC with marked recording locations. b) Simultaneously recorded spike trains from S1BF, V2L, PER, and HPC single units during a visual trial. Units are ordered according to average firing rate and grouped per recording region. See panel a) for color coding of brain regions. c) Overview of task-phase modulation in S1BF, V2L, PER, and HPC cells. The histograms indicate the percentage of cells that discharged maximally on a given time point. The heatmaps are Z-scored firing rates of cells over time, which are linearly time-warped to account for unequal durations in object sampling and response latencies. Cells are ordered by the moment of peak firing rate relative to sample onset. The vertical lines represent the median time points derived from all trials, which were later used for the linear warping of firing rates. The light gray lines correspond to the duration spanning from the initiation of object sampling to the point of retraction from the object. The sampling period is marked by the initiation of object sampling up to the start of locomotion toward the reward ports. Red: NPR, directly followed by reward delivery in a correct trial. d) Percentages of cells from a given area that preferentially discharged during object sampling. Bars are 95% CIs, dashed lines indicate chance levels given homogeneously distributed events over time. Asterisks indicate significant above-chance percentages. S1BF: 11.8%; V2L: 11.9%; PER: 6.7%; HPC: 9.3%. e) Percentage of cells from a given area that preferentially discharged following the NPR, regardless of reward delivery, up to 1 s after poke (S1BF: 17.6%; V2L: 17.2%; PER: 28.1%; HPC: 11.3%). Bars indicate 95% CIs, * for significantly higher percentages than uniformly distributed events ($P < 0.05$, 2-proportions z-test).

(such that PER neurons are responsive to more than one modality), we characterized neural responses during tactile, visual, and multisensory object sampling. Using AUROC analysis, we quantified the proportion of cells significantly modulated by either light onset or whisker-object contacts.

Neural responses to the illumination of the object were initially quantified within the first 0.2 s after light onset. To mitigate potential motor-related confounds associated with locomotion and sampling behavior, responsiveness to light onset was defined as an augmented firing rate in visual or multisensory trials compared with tactile trials wherein no light was triggered during object sampling behavior. This criterion was applied because the sampling behavior between these trials was very similar, reducing the likelihood of motor-related confounds. We found significant proportions of cells in area V2L and HPC that were modulated during visual object sampling (before the animals retracted from the object; Fig. 3a to d; percentages of cells modulated by light onset in absence of simultaneous tactile sampling: V2L: 39.0%, $Z = 10.75$, $P < 0.001$; HPC: 13.7%, $Z = 2.98$, $P = 0.010$, and during simultaneous visual and tactile sampling: V2L: 31.0%, $Z = 8.84$, $P < 0.001$; HPC: 13.7%, $Z = 2.98$, $P = 0.010$, proportions z-test, Bonferroni corrected). Responses to light onset were suppressed in multisensory trials compared with visual-only trials in a significant proportion of V2L cells (Fig. 3e; V2L suppressed: 10.9%, $Z = 2.58$, $P = 0.020$; V2L enhanced: 4.4%, $Z = 0.87$, $P = 0.780$; HPC suppressed: 21.1%, $Z = 1.98$, $P = 0.095$; HPC enhanced: 10.5%, $Z = 1.14$, $P = 0.509$, proportions z-test, Bonferroni corrected). Individual cells in S1BF and PER were not modulated by light onset (Fig. 3b to d; S1BF: 6.8%, $Z = 0.60$, $P = 1.00$; PER: 5.9%, $Z = 0.456$, $P = 1.00$, proportions z-test, Bonferroni corrected).

Next, we analyzed modulation of firing patterns by tactile sampling on a relatively coarse time scale (from start of sampling up to retraction, defined by means of high-speed video tracking at 500 frames/s; see Fig. 4a and b, for example, cells). On this time scale a significant proportion of S1BF and HPC neurons responded to whisker touch (Fig. 4c; percentages of cells modulated by touch in absence of light: S1BF: 19.3%, $P = 0.016$, $Z = 2.87$; HPC: 28.1%, $Z = 5.78$, $P < 0.000$, and modulated when combined with light: S1BF: 18.0%, $Z = 2.65$, $P = 0.032$; HPC: 29.5%, $Z = 6.08$, $P < 0.000$, proportions z-test, Bonferroni corrected). We found no marked responses to whisker touch in PER and V2L when tested on this coarse time scale (percentages of cells modulated by touch in absence of light: V2L: 10.2%, $Z = 2.22$, $P = 0.152$; PER: 6.1%, $Z = 0.41$, $P = 1.00$, and modulated when combined with light: V2L: 7.7%, $Z = 1.23$, $P = 0.873$; PER: 2.4%, $Z = -1.15$, $P = 1.00$).

We additionally quantified responses to individual whisker-object contacts by AUROC analysis of firing rate responses in the first 50 ms after individual touches. At this fine time scale, cells in S1BF were significantly modulated by touch, whereas cells in other regions were not (Fig. 4d and e; S1BF: 22.2%, $Z = 3.93$, $P < 0.001$; V2L: 5.0%, $Z = 0.014$, $P = 1.00$; PER: 5.3%, $Z = 0.179$, $P = 1.00$; HPC: 2.7%, $Z = -1.904$, $P = 1.00$, proportions z-test, Bonferroni corrected). Subdividing HPC cells into the different subregions of origin (CA1, CA3, DG) did not reveal significantly different proportions of responsive cells between subregions for touch or light onsets ($P = 1.00$, proportions z-test, Bonferroni corrected); therefore, these HPC cells were pooled. The main result from these analyses is that tactile and visual responses evoked at stimulus onset—although expressed in S1BF (Fig. 4e) and V2L (Fig. 3d)—do not emerge in PER when rats sampled objects through vision and/or touch, despite the finding that such responses are, in fact, expressed in HPC (Figs. 3d and 4c).

Neural correlates of object identity

The PER is sometimes considered a terminal area of the visual cortical stream, involved in object (or item) perception and recognition memory (Norman and Eacott 2004; Bussey and Saksida 2005; Bartko et al. 2007; Dickerson and Eichenbaum 2010). To obtain reward during our task, the rats needed to sample and recognize the objects by vision and touch. We first quantified how object identity was represented by individual cells in the hierarchy using a GLM that included choice side and object identity as predictors. The GLM quantified the influence of both predictors on neural responses over time, based on the instantaneous firing rates during all trials, aligned on sample start. We did this separately for tactile, visual, and multisensory sampling, assuming that neural representations may differ depending on the sensory modality at hand. Cells were considered to be modulated by object identity if the GLM object coefficient magnitude was larger than what would be observed by chance, within 0.5 s after initiation of object sampling. This epoch was chosen because high object predictor magnitudes clustered during this epoch, and the choice side predictor became dominant thereafter (Fig. 5). In short, object identity was defined by the response distinguishing between 2 objects during the sampling behavior in a given modality, with the potential confounding factor of choice side effectively eliminated through regression analysis. V2L cells expressed significantly different responses depending on object identity during visual, but not tactile sampling (Fig. 5d and f; visual: 9.2%, $Z = 2.34$, $P = 0.04$; tactile: $P = 1.00$; proportions z-test, Bonferroni corrected). From these object encoding V2L neurons, 69.8% preferentially fired in response to object A, whereas the remaining cells preferentially responded to object B. In contrast, S1BF, PER, and HPC cells were not encoding the object identity during visual sampling behavior at all (Fig. 5e and f, S1BF: 5.1%, $Z = 0.05$, $P = 1.00$; PER: 3.6%, $Z = -0.93$, $P = 1.00$; HPC: 3.5%, $Z = -0.96$, $P = 1.00$). We did not find above-chance proportions of cells that encoded objects during tactile-only trials in any of the recorded regions ($P > 0.05$ for all regions, proportions z-test, Bonferroni corrected). Additional control analysis confirmed that V2L cells with significant GLM object predictors tended to have higher AUROC values for object identity than for choice side ($T(618) = -5.16$, $P < 0.001$; independent t-test). We verified that object correlates did not emerge later in time by applying the same analysis to a longer time window (0.5 to 2 s post-sampling). Thus, whereas single V2L cells coded object identity during visual object sampling, this coding was surprisingly absent in single units recorded in PER and HPC.

We additionally quantified if object information was represented through the collective activity of cell populations within a specific area. We constructed pseudo-populations that consisted of rate vectors from 100 neurons obtained from different sessions for each area separately. A decoder was trained to classify the object within each specific combination of modality and choice side. The accuracy of classification was assessed over time using cross-validated predictions. We subsequently computed the average classification accuracies for the 2 choice sides within a modality. This allowed us to obtain an object population decoding accuracy within a given modality and eliminating the influence of the choice side. In line with the single-unit GLM analysis results, we found a population code for the object identity in V2L during visual object sampling, but not during tactile sampling (Fig. 6a, $P < 0.05$, tested against permutation-based surrogate distribution). Conversely, neural populations in S1BF briefly coded for the object identity after sampling onset only in the tactile

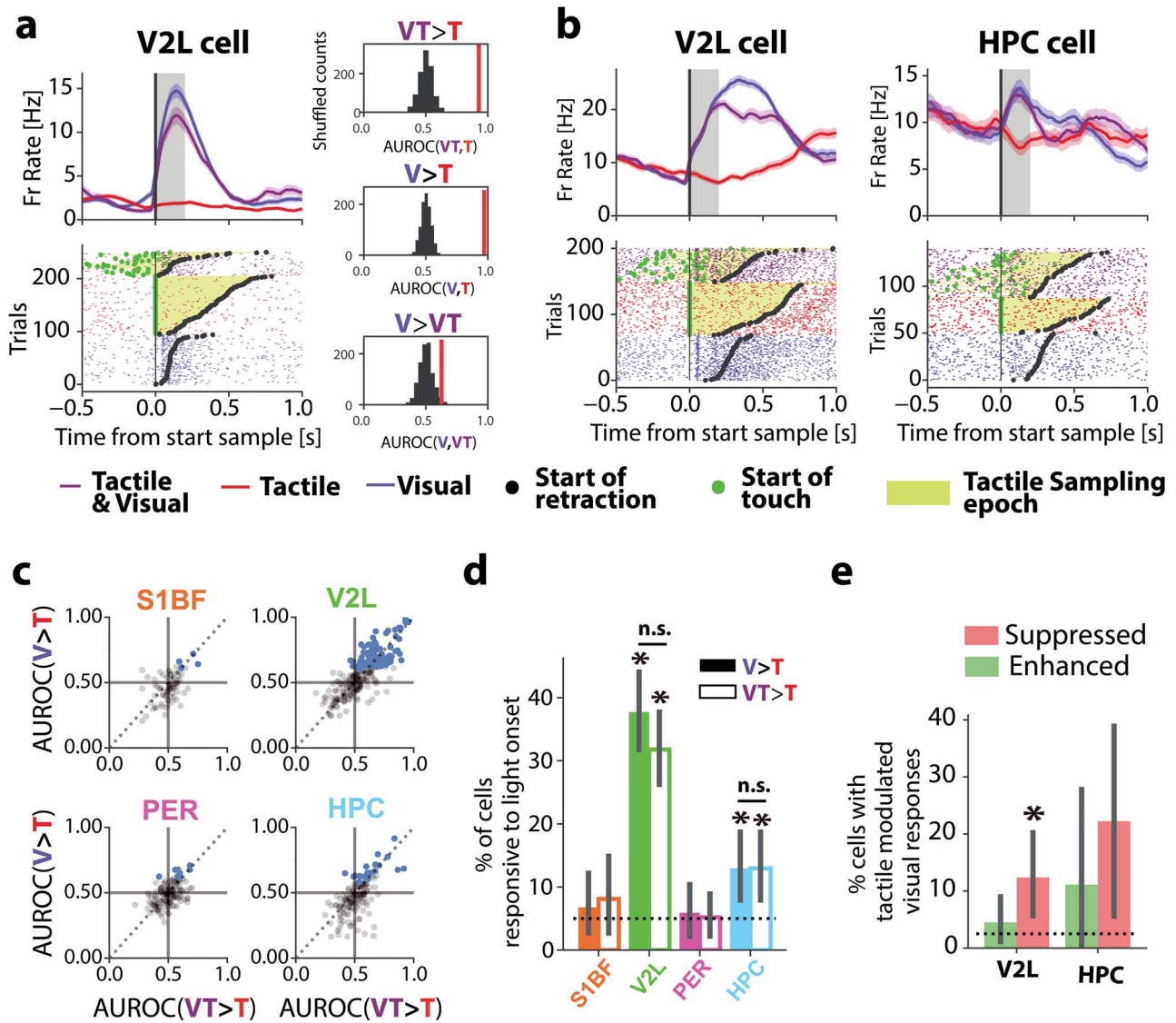


Fig. 3. Visual responses of neurons recorded in all 4 areas during object sampling. **a, b** Example cells modulated by light onset. Peristimulus time histograms (PSTHs; top) and spike rasters (bottom) aligned on the start of object sampling are contrasting visual (blue), tactile trials (red), and multimodal (purple) trials. Light onset responses were quantified across the 3 different sampling conditions to account for potential confounds related to modality-specific sampling behavior. Multisensory trials are aligned to the light onset and the first touch in a trial is indicated by a green dot in the rasters. Retraction moments are marked by a black dot. This color coding holds in **a, b, f**, and **g**. Vertical gray bar: time window used for analysis of light onset modulation. **a** Right side: observed AUROC values (red) for firing rate differences for the example V2L cell and trial modality label shuffled chance level distributions (black). The values were measured by AUROC analysis on firing rates during the first 0.2 s after the light onset (gray shaded area). Cells with an AUROC value above 95% CIs of the shuffled distribution were considered to be significantly responsive to light onset. This example cell was modulated by light onset during tactile sampling ($VT > T$) as well as by light onset in absence of any whisker input ($V > T$). Tactile sampling suppressed light onset responses ($V > VT$). **b** Two other example cells modulated by light onset. **c** Overview of AUROC values for light onset responses of all cells per brain region. The majority of cells with significant AUROC values for light onset were observed in V2L, most often by responding to light onset in multisensory trials (x axis, $VT > T$) as well as in visual trials (y axis, $V > T$; blue dots indicate cells significant for at least 1 of the 2 modality contrasts). **d** Percentage of cells per area which were modulated by light onset measured by AUROC analysis. Light onset was quantified by contrasting light onsets with combined touch to trials with touch in darkness ($VT > T$; empty bars; S1BF: 6.8%; V2L: 34.0% PER 5.9%; HPC: 13.7%), or by contrasting light onsets in absence of touch to trials with only touch ($V > T$; filled bars; S1BF: 8.1%; V2L: 30.9%; PER 6.7%; HPC: 13.7%). Black bars indicate 95% CIs. Asterisks indicate that the percentage of significant cells was higher than chance, ($P < 0.05$, 2-proportions z-test). This holds in **e, h**, and **j** as well. **e** Percentage of light onset responsive cells in V2L and HPC that showed tactile modulations of the light onset response (S1BF and PER are not shown because of lack of significant modulation, see **d**). For all cells that were significantly responsive to light onset ($V > T$), tactile modulation of the light onset response was quantified by contrasting visual responses with combined touch (VT) to visual responses in absence of touch (V2L suppressed: 10.9%; V2L enhanced: 4.4%; HPC suppressed: 21.1%; HPC enhanced: 10.5%).

trials, but not in the visual trials (Fig. 6b, $P < 0.05$, tested against permutation-based surrogate distribution). PER and HPC did not represent object identity during the first 2 s following the start of object sampling (Fig. 6c).

Neural representations of the object identity may not only emerge upon initiating the object sampling, but might additionally arise upon recalling object information later in the

trial. We therefore performed additional population decoding analysis on firing rates aligned on 3 distinct time points. These included the onset of object sampling, the decision moment of the rat, and the onset of the object-associated NPR. The decision moment was defined as the moment at which a rat stopped sampling the object and initiated its choice toward the left or right side (detected by high-speed video tracking of the snout).

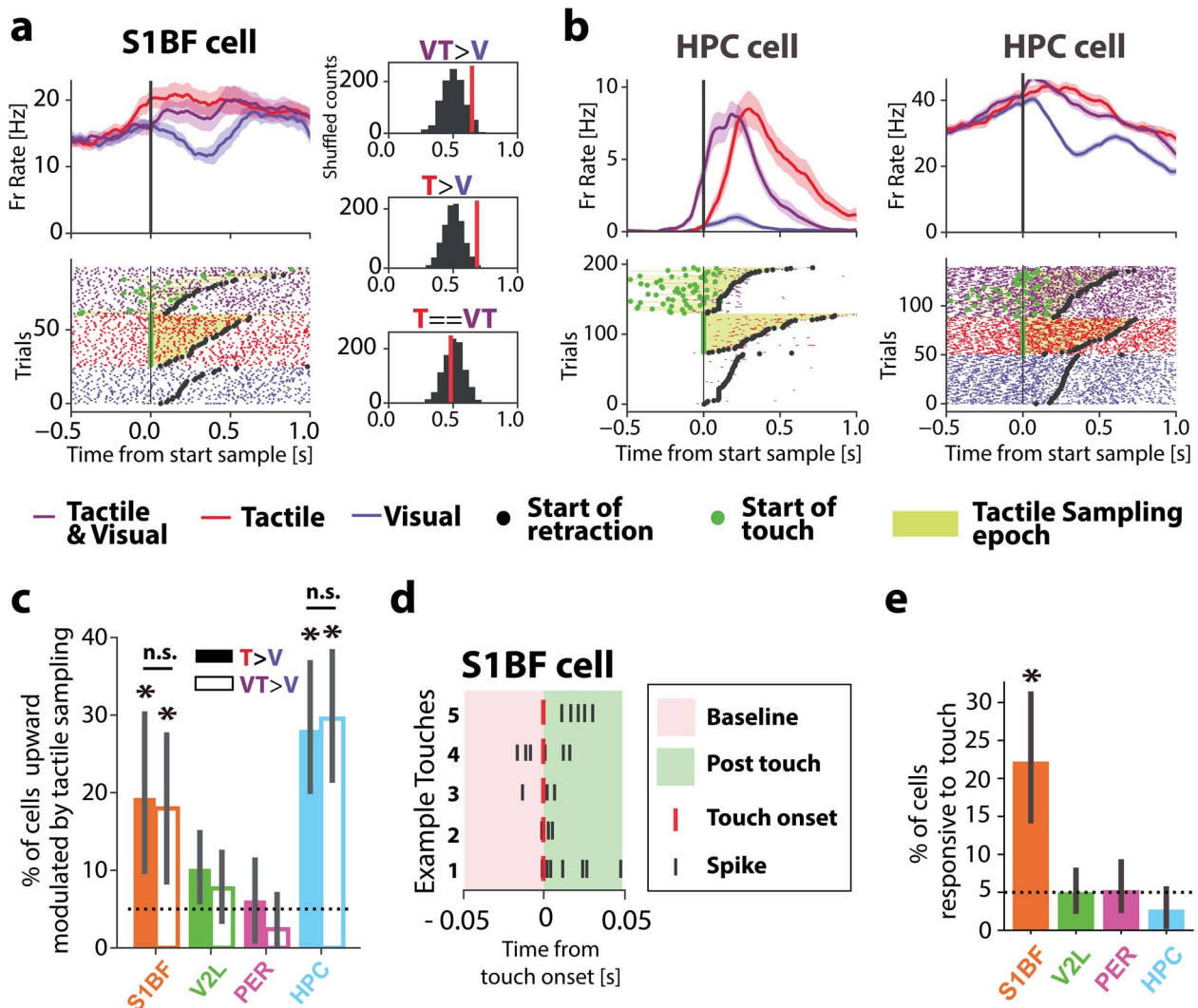


Fig. 4. Tactile responses of neurons recorded in all 4 areas during object sampling. **a, b** Example cells modulated by tactile sampling. PSTHs (top) and spike rasters (bottom) contrasting visual (blue), tactile trials (red), and multimodal (purple) trials. Multisensory trials are aligned to the light onset. The first touch in a trial is indicated by a green dot in the rasters. Retraction moments are marked by a black dot. **a** Right side: observed AUROC values (red) for firing rate differences for the example S1BF cell and trial modality label shuffled chance level distributions (black). The values were measured by AUROC analysis on firing rates during sampling, up to retraction from the object. Cells with an AUROC value above 95% CIs of the shuffled distribution of the VT vs. V comparison were considered significantly responsive to tactile sampling because these trials had identical illumination conditions. This example cell was modulated by tactile sampling regardless of the illumination (VT > V and T > V). Tactile responses were not modulated by the light onset (T = VT). **c** Percentage of cells per area showing firing-rate enhancement by touch onset under identical illumination conditions (VT > V: empty bars; S1BF: 18.0%; V2L: 7.7%; PER: 2.4%; HPC: 29.5%) and under different illumination (T > V: filled bars; S1BF: 19.3%; V2L: 10.2%; PER: 6.11%; HPC: 28.1%), as measured by AUROC analysis on firing rates during sampling up to retraction from the object. Bars indicate 95% CIs. **d** Spike times aligned to example touches (red) from one example S1BF cell. Touch onset responses were measured for each cell by contrasting the 50 ms following each touch onset (green background), with the 50 ms preceding the onset (red background). **e** Percentage of cells per area that are modulated by touch onset in the first 50 ms after touch onset (S1BF 22.2%; V2L 5.0% PER 5.0%; HPC 2.5%). Bars indicate 95% CIs.

The onset of the NPR is the moment at which rats entered their snout in the reward port and received feedback on their choice through reward delivery for a correct response or the omission of reward for an incorrect choice. Neural populations in higher-order regions such as the PFC and the HPC have been shown to represent task variables in an abstract manner, emphasizing their ability to generalize across diverse cognitive contexts and conditions. We therefore trained a decoder to classify trial types based on all trial combinations of object identity, sensory modality of sampling, and chosen side. Trial types were counterbalanced to ensure an equal distribution of trials for each type in the training data. The accuracy of classification for choice, modality, and object was assessed over time using cross-validated predictions, which were then organized into a confusion matrix

(Fig. 6d, see also Materials and Methods). Consequently, high object decoding accuracies mean that a decoder can accurately classify the object's identity regardless of the sensory modality. The classifier failed to extract object identity based on PER or sensory cortex population activity, but revealed above-chance classification accuracies for the HPC after the NPR (Figs. 6f and S4, $P < 0.05$, tested against permutation-based surrogate distribution). The population decoding additionally replicated the earlier single unit analysis on sensory modulations by demonstrating a high accuracy in classifying the sensory modality based on the population activity within regions S1BF, V2L, or HPC (Figs. 6e and S4, $P < 0.05$, tested against permutation-based surrogate distribution). However, it failed to accurately discern the sensory modality based on population activity within the PER

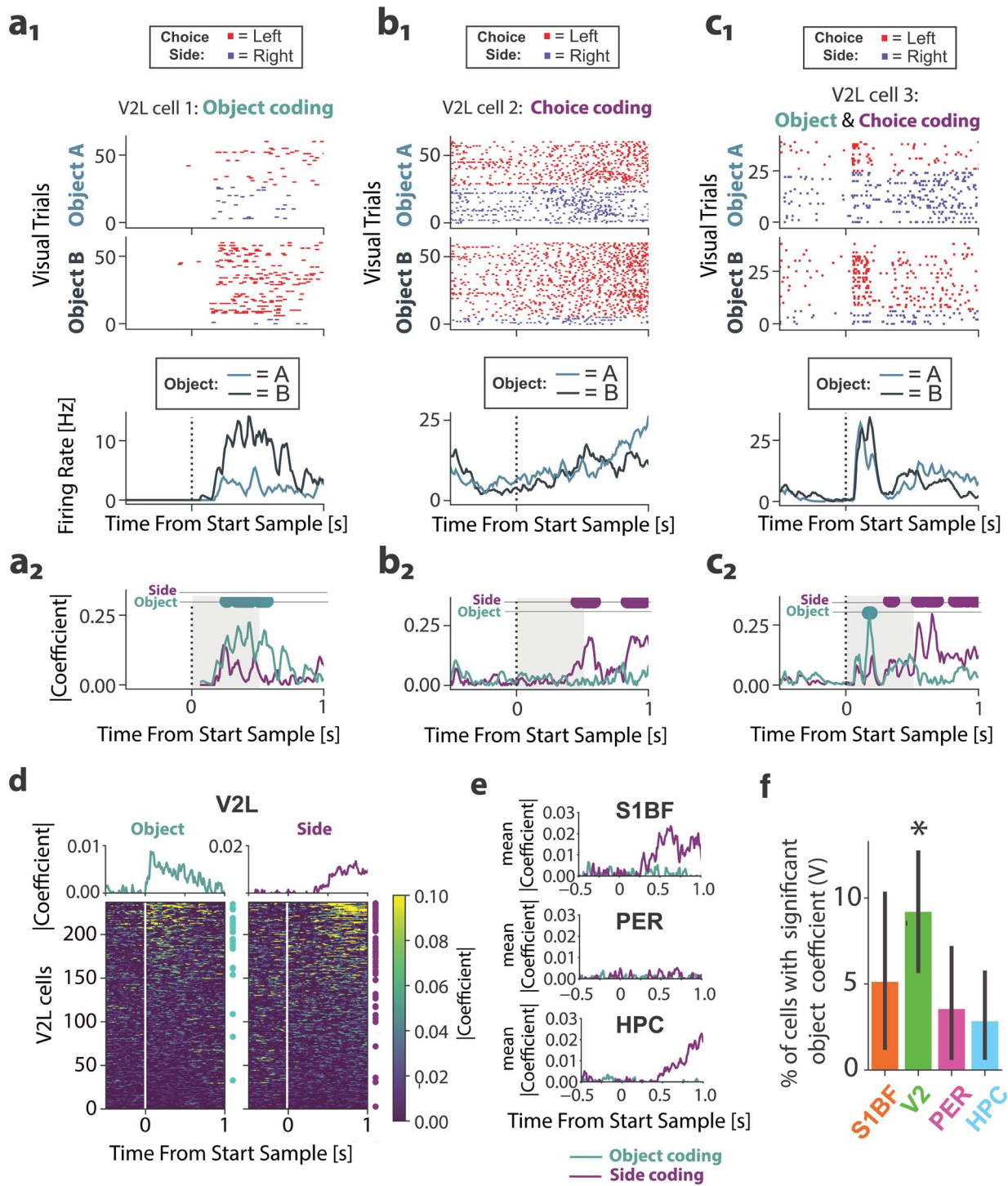


Fig. 5. Visual object coding by single cells in V2L, but not in PER, S1BF, or HPC. a1 to 2) Example V2L cell that is coding for object identity. This cell's response to object B cannot be explained by choice behavior: note the raster differences between the 2 objects for only the left choice trials (for this rat the left choice was associated to object B). Top panels: spike rasters of visual trials grouped by object identity, and color coded according to response side. Bottom panel: mean firing rates over time for trials in which object A was presented vs. trials presenting object B (visual trials only). Shaded bands indicate SEM. b1 to 2) example V2L cell that is coding for choice side, but not for object identity. c1 to 2) Example V2L cell that first codes for object identity, and codes for choice side thereafter. a2, b2, c2) Absolute magnitudes of the GLM coefficients for the choice side and object identity for the same cells as in a1 to c1. Colored dots above coefficients indicate significant encoding of the object identity (cyan) or choice side (purple; $P < 0.05$ Benjamini-Hochberg corrected). The shaded gray areas indicate the time window used for subsequent calculation of object coding indices in f. d) Time course of object coding dominance and choice coding dominance in V2L. Heatmaps display the difference in predictor coefficient magnitude over time for all 237 V2L cells (left: object, right: choice). Colored dots on the right side of a heatmap indicate cells for which the object predictor (cyan) or choice-side predictor (purple) contributed significantly to the firing rate variance on any time point within the 0.5 s after starting to sample. The cells are ordered according to the maximal dominance of a given predictor (left: object dominance, right: choice dominance). e) Time course of the average difference in predictor coefficient magnitude from all S1BF, PER, and HPC (compare to V2L, upper panels of d). f) Area-specific percentages of cells with significant GLM-based object modulation in visual trials (S1BF: 5.1%; V2L: 9.2%; PER: 3.6%; HPC: 3.5%). Bars indicate 95% CIs. * indicates percentage of significant cells higher than chance ($P < 0.05$, 2-proportions z-test).

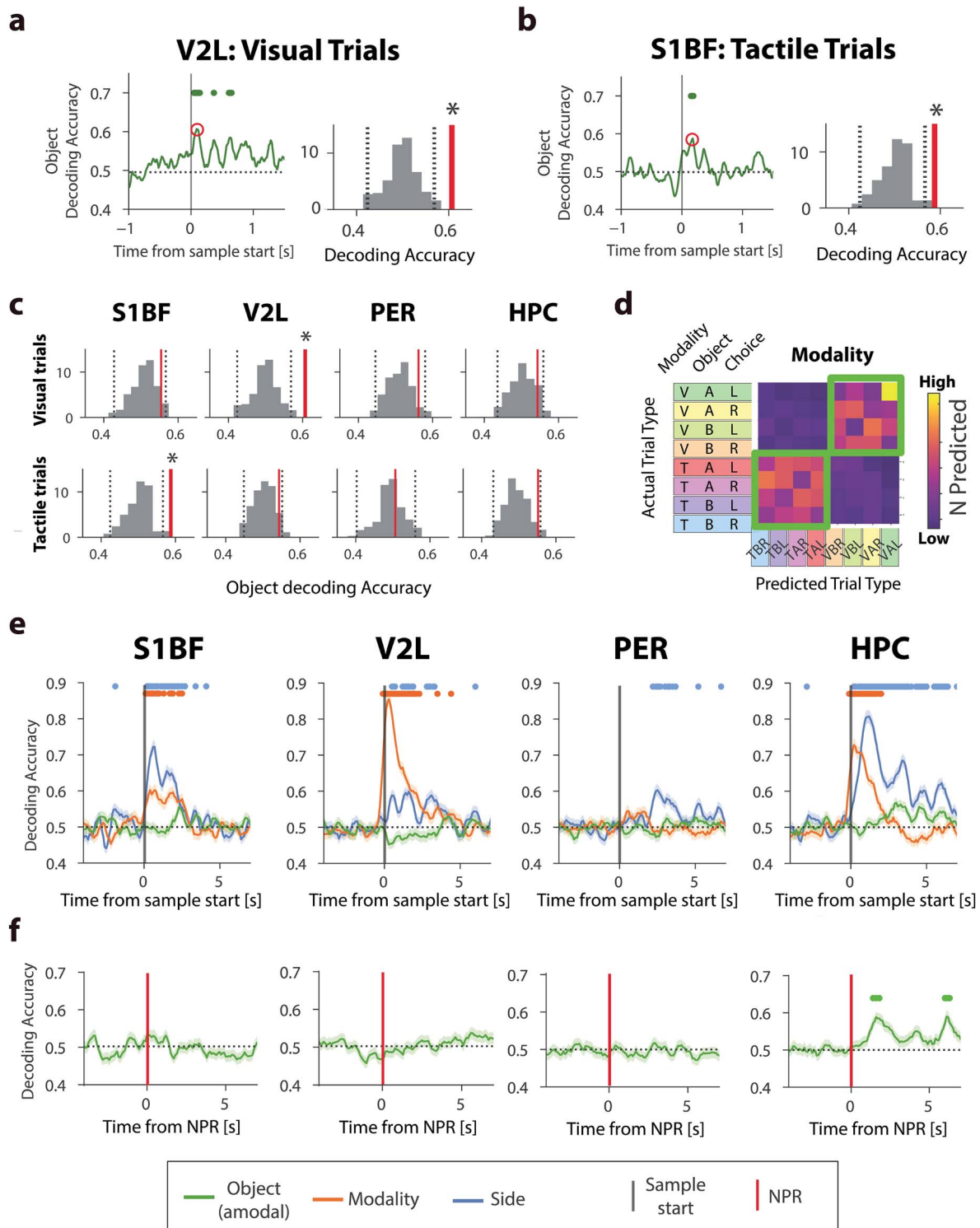


Fig. 6. Population decoding of object identity and trial type. a) Left side: object population decoding accuracies over time for V2L obtained through training and testing within visual trials. Green dots indicate above chance object decoding accuracies. The red circle highlights the highest object decoding accuracy. Right side: probability density histogram of decoding accuracies derived from shuffled distributions. The highest observed object decoding accuracy is in red. Dashed lines are 95% CIs based on shuffled distributions b) same as for a, but now for S1BF population activity during tactile trials. c) Modality-specific object decoding accuracies obtained through training and testing within visual (top row) and tactile trials (bottom row). Histograms are probability densities of decoding accuracies derived from shuffled distributions. Red lines indicate the maximum object decoding accuracy after the sampling onset, obtained by decoding over time using a sliding window. Dashed lines are 95% CIs based on the shuffled distributions d) schematic illustration of trial type classification accuracy assessment based on contingency matrices. The population decoder was trained to predict trial types based on the presented objects (A vs. B), the choice sides (L, left vs. R, right), and the sensory modality (V, vision vs. T, touch). This contingency matrix is from area V2L and illustrates high modality classification shortly after the start of sampling. Green outlines are the correct predictions for the sensory modality. e) Time course of decoding accuracy for the classification of trial types based on population activity in S1BF, V2L, PER, and HPC. Colored dots indicate significant classification accuracies. f) Same as b, but now only for the amodal object trial label, and based on firing rates aligned on the NPR (red vertical line).

(Figs. 6e and S4, $P > 0.05$, tested against permutation-based surrogate distribution). The decoder additionally demonstrated a high accuracy in predicting the chosen side based on the population activity patterns within each of the regions during both tactile and visual trials (Figs. 6e and S4, $P < 0.05$, tested against permutation-based surrogate distribution). This observation highlights a widespread representation of the choice side that remained consistent across sensory modalities; although the exact nature of this representation might either originate from corollary discharge, vestibular-proprioceptive inputs, or from spatial coding. Choice side decoding based on PER population activity was comparatively less robust and manifested at a later stage than in the other regions. Notably, this decoding performance appeared to be concentrated around the median time points of the NPR (Fig. S4).

To further quantify modality-independent object representation, we investigated the extent of generalization within the population code by training and testing a decoder across distinct sensory modalities (Bernardi et al. 2020). We initially trained a decoder to classify objects based on neural activity from tactile trials. Subsequently, we evaluated the decoder's ability to classify objects using neural activity derived from visual trials (Fig. 7a). To eliminate potential biases by the choice sides, left and right choice side trials were counterbalanced within the training and testing data sets. Moreover, we extended the analysis to encompass a more extended time period following the NPR, aiming to assess the duration of the previously observed amodal object population code in the HPC. In this cross-modal population decoding analysis, we generated pseudo-populations composed of rate vectors from 100 neurons, gathered from various sessions, for each area individually. Decoding based on the neural data in the HPC revealed significant decoding accuracies for cross-modal object classification after the NPR, but not before. This generalized object population code persisted throughout the duration of the ITI—although with some interruptions—until the onset of the subsequent trial in the case of a correct response ($P < 0.05$, tested against permutation-based surrogate distribution; Fig. 7b; ITI following a correct response is 12 s). The decoder failed to classify the object across sensory conditions based on population activity in the PER, or in the sensory cortices ($P > 0.05$ tested against permutation-based surrogate distribution; Fig. 7c). Despite the absence of clear object representations in the PER's population code when decoding within trial types (Fig. 6a to c) or across conditions (Fig. 7), or when pooling tactile and visual trials together (Fig. 6d to f), it remains possible that the PER represents the objects exclusively upon combined tactile and visual input. We therefore verified that this was not the case by training and testing a classifier based on neural activity from only the multisensory trials. Decoding within only multisensory trials did not reveal a population code for object identity in PER ($P > 0.05$, tested against permutation-based surrogate distribution). Hence, a modality-independent population code for objects emerged within the HPC during the ITI upon reward-based feedback. Remarkably, this representation occurred in the absence of concurrent object representation in PER.

Perirhinal neural correlates of choice side temporally align to reward site visits

In addition to the anatomical connections between PER and sensory cortical regions, PER also receives projections from subcortical motivation-related structures such as the substantia nigra, ventral tegmental area, and amygdala, as well as from medial

PFC (Burwell et al 1995; Kajiwar et al. 2003; Agster et al. 2016). Previous studies demonstrated that PER cells carry spatial information during choice behavior in a task environment (Bos et al. 2017) and differentiate between choice sides most strongly at goal-specific locations (Ahn and Lee 2015). As, in our task, high accuracies in choice side predictions based on PER population activity concentrated around the median time points of the NPR (see above), we set out to examine the temporal modulation of PER choice side correlates in more detail. Corollary discharge and vestibular-proprioceptive inputs may be expected to arise upon initiation of locomotion toward reward goals, whereas representations of goal locations may arise upon arrival at the reward ports. We first verified that PER cells were not affected by the choice side during locomotion initiation by AUROC analysis of firing rates of neurons during turns toward the different directions. We found that PER firing rates were not affected by choice side when rats initiated a turn toward the goal locations for reward when they retracted from the object (interval: 0 to 1 s from sample start; Fig. 8b). This absence of choice side coding contrasted to modulations observed in the HPC and the sensory regions, which did reflect changes in snout positions during opposed directions of self-motion when retracting from the object.

Contrasting with the lack of specific coding during object sampling and retraction, we did in fact observe that PER cells preferentially discharge after the NPR (Figs. 2c and e and S3; probabilities, S1BF: 0.176, $Z = 1.24$, $P = 0.426$; V2L: 0.172, $Z = 2.02$, $P = 0.086$; PER: 0.281, $Z = 4.63$, $P < 0.001$; HPC: 0.113, $Z = -0.50$, $P = 1.00$, tested against chance level of uniformly distributed events, proportion z-test, Bonferroni corrected). Because of the self-paced nature of the task, rats exhibited variable delays between initiation of locomotion and the arrival at reward locations across trials. To examine how the temporal modulation of choice side related to the arrival at the reward locations, we applied a linear time-warp to the neural data from locomotion initiation to reward location arrival. We then constructed pseudo-populations for each area separately as described earlier, but now restricted the classification to the choice sides only and performed the analysis on visual and tactile trials separately. The choice side of the animal was accurately decoded from the population responses from S1BF, V2L, and HPC as soon as the animals initiated their choice response, both in darkness and light. In PER, decoding accuracy of choice side was generally lower during locomotion, but peaked after the first NPR (Fig. 8c).

Multiple task variables could potentially affect firing rates of individual cells during choice behavior. To disentangle the contribution of photic condition, choice (Left/Right), reward, and object coding, we examined the relation between each of these task variables and neural responses with a GLM. Cells were considered to be selective for choice side if the GLM fit resulted in a significant choice side coefficient at any moment in the trial (see Materials and Methods). PER choice side coefficients preferentially peaked following the NPR, whereas cells in other regions differentiated between sides most prominently during the preceding locomotion toward the goal location (Fig. 8d; fraction of choice encoding cells preferentially firing for the left over the right side: S1BF: 0.557; V2L: 0.378; PER: 0.622; HPC: 0.527). In total, 12.2% of PER cells encoded the choice side within 1 s after the NPR, as opposed to 8.0% in the second just before NPR entry. These results show that PER neural responses are more strongly correlated to the moments of (expected) reward delivery, compared with the HPC and sensory regions, which were modulated by choice side most strongly during locomotion.

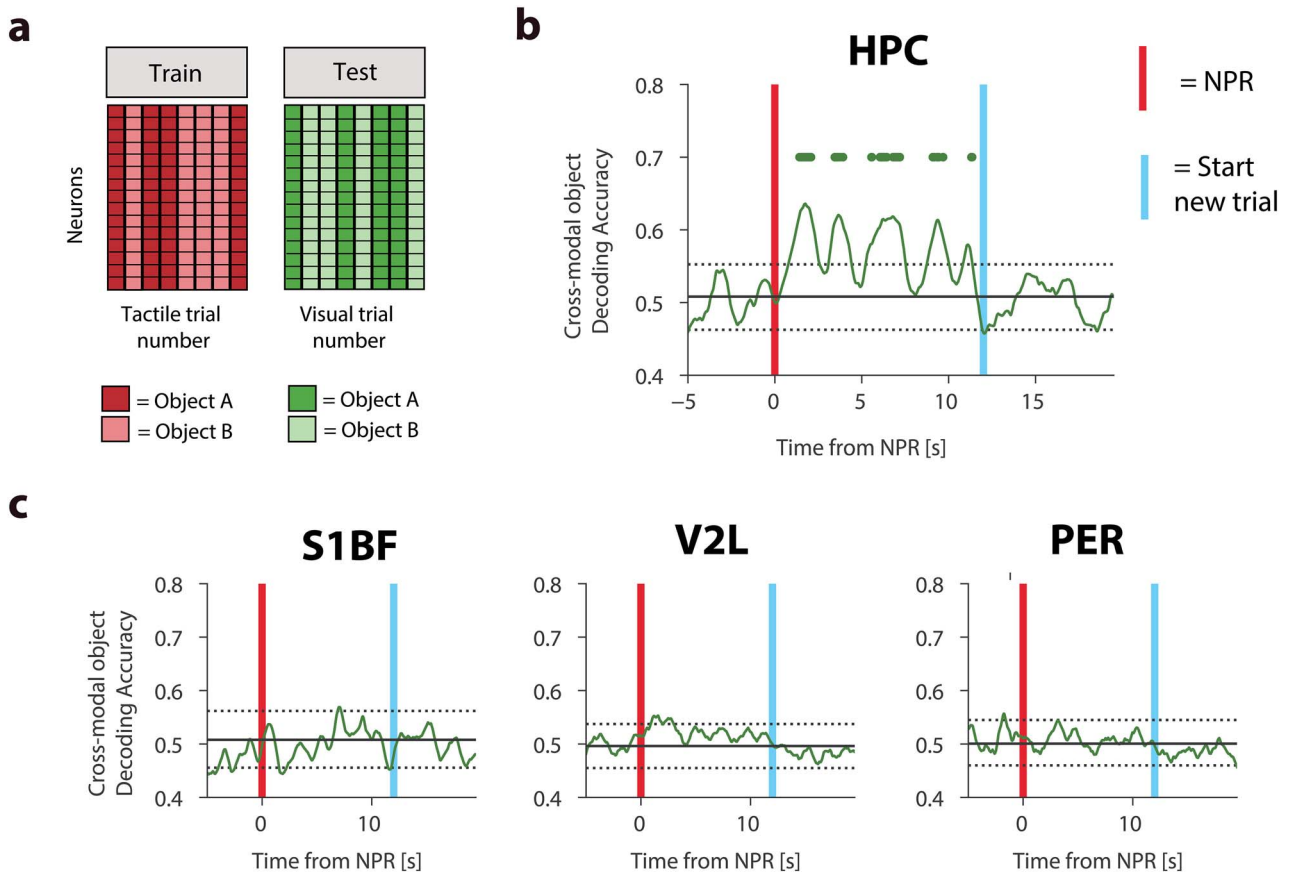


Fig. 7. Cross-modal population decoding of object identity a) schematic illustration of cross-modal object classification based on population activity. A population decoder was trained to classify objects based on neural activity during tactile trials. The decoder's ability to generalize across sensory modality was tested by classifying objects based on the activity of the same cells during visual trials. b) Time course of cross-modal object decoding accuracy based on population activity from HPC, aligned on the NPR (red line). The cyan line marks the onset of a new trial after a fixed ITI of 12 s following a correct response. Green dots indicate significant cross-modal object classification accuracies. Dashed lines are 95% CIs based on shuffled distributions. c) Same as for b, but now for S1BF, V2L, and PER.

PER encodes choice and trial outcome during reward sampling

Our results indicate that PER cells preferentially discharge after the poke for reward, and that the PER increasingly starts to differentiate between choice sides when rats arrive at the goal locations for reward. The PER might integrate information on expected reward for a specific goal location with information on the actual outcome, reminiscent of prediction values, and prediction errors in temporal difference reinforcement learning (TDRL) algorithms and related models (Schultz et al. 1997; Sutton 1988; Pennartz 1995; Sutton and Barto 1981). Therefore, we scrutinized the period in which the rats experienced the actual trial outcome based on nose poke and lick behavior. This IOP started when rats poked the reward port, after which they were confronted with the delivery of reward or the omission of it. The rats' reactions were then measured by means of the first lick after the NPR, which was the moment that rats started to sample for the outcome. The IOP lasted until rats had started to sample for reward delivery by licking in 95% of all trials. Importantly, lick rate adjustments to the availability of reward (delivery vs. omission) occurred subsequently to this epoch (Fig. 9a). Thus, any differences in firing rate between rewarded and unrewarded trials after the IOP could not be differentiated from reward-associated motor activity (e.g. licks and reward port exits), whereas firing rate modulations during the IOP were unlikely driven by these

confounds. Upon inspection of individual neurons, we noted that a subset of PER cells transiently increased their firing rates during the IOP depending on the actual trial outcome (Fig. 9b). In the other regions, cells generally fired according to the outcome only after the IOP and in a more sustained way (Fig. 9c). We employed a GLM on the reward phase to disentangle the contributions of trial outcome, photic condition (object-focused light off or on), and object identity to time-dependent modulations in firing-rate distributions for each individual neuron (Figs. 10a to c and S5). We quantified whether individual cells carried information about trial outcome earlier in PER than in other regions by comparing the summed reward coefficient magnitude over time between significant cells from the different regions. During the IOP, outcome coefficient magnitudes increased earliest in PER (Fig. 10d). PER cells had higher outcome magnitudes during the IOP compared with a pre-poke baseline (Fig. 10d; $P = 0.001$; 1-way ANOVA [$F = 8.385$, $P < 0.001$], with post hoc Tukey test). Similarly, the number of cells that preferentially encoded the outcome during the IOP was higher than expected by chance only in the PER, whereas cells in other regions generally responded thereafter, during outcome-dependent behavioral adjustments (Fig. 10e and f; $P < 0.05$; proportion z-test, Bonferroni corrected; S1BF: 7.9%, $Z = -2.46$, $P = 0.99$; V2L: 10.9%, $Z = -1.72$, $P = 0.96$; PER: 30.3%, $Z = 2.08$, $P = 0.02$; HPC: 1.6%, $Z = -10.52$, $P = 1.00$). During the IOP, the firing rate of individual PER cells did not correlate to

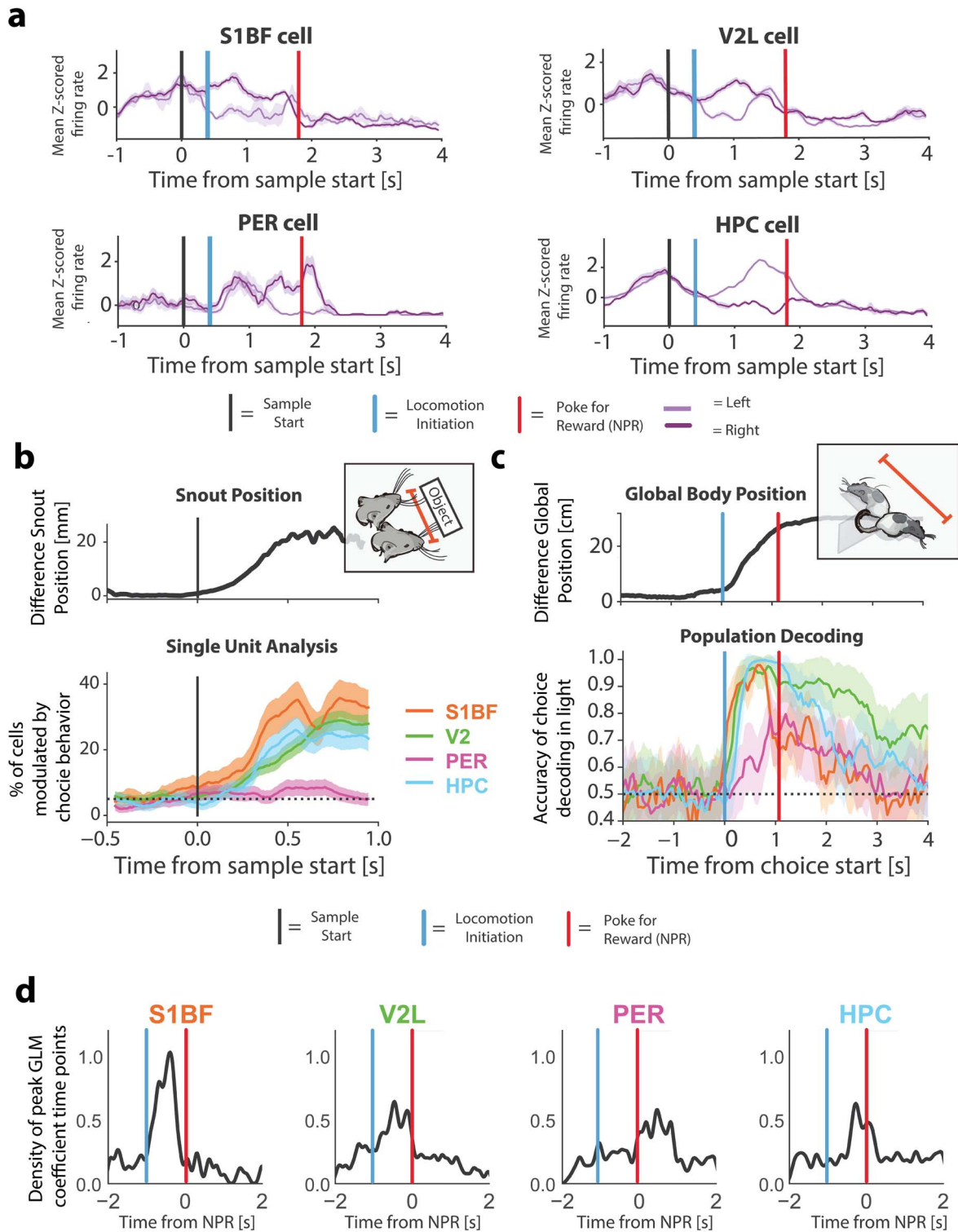


Fig. 8. Temporal dynamics of choice side coding. S1BF, V2L, and HPC cells were modulated mainly during the choice phase, whereas PER cells were mostly modulated during the outcome phase. **a)** Z-scored firing rates of example cells in the cortico-hippocampal hierarchy. Firing rates are linearly warped to align on the start of object sampling (black), the end of sampling, coinciding with the start of locomotion toward the left or right side (blue), and the NPR (red) to account for unequal durations in object sampling and response latencies. **b)** Top: average difference in snout position between left and right choice trials during object sampling behavior. Rats initiated a sideways motion toward the chosen side already within 1 s after sampling onset. Bottom: percentage of cells significantly modulated by choice side, plotted as a function of time. Initial sideways motion toward the chosen side was represented prominently by cells in the sensory cortices and HPC, but not by cells in the PER. **c)** Top: mean global body position difference of 2 example rats on the elevated platform during choice behavior (black). Bottom: temporal dynamics of population decoding accuracy of choice side, based on firing rates linearly warped for temporal alignment on the end of the sampling, marked by retraction from the object and the start of the left or right choice turn, and the poke for reward. **d)** Densities of NPR-aligned times at which cells maximally differentiate between the choice sides, based on coefficients from a GLM that included choice side, object identity, sensory modality, and trial outcome as predictors. Only cells with a significant choice side predictor are included in the densities. The vertical lines represent the median time points derived from all trials from all sessions.

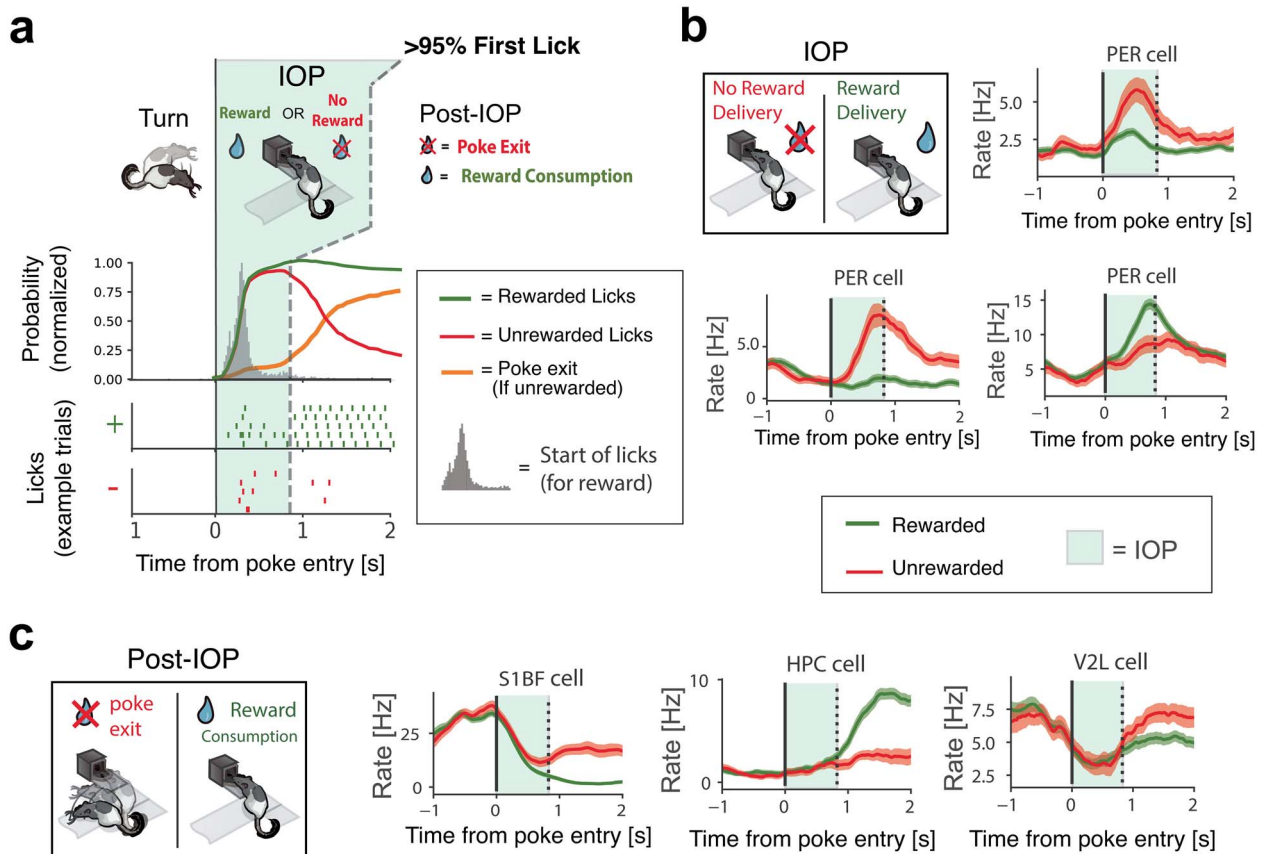


Fig. 9. Trial outcome selectivity of perirhinal cells during reward delivery. a) Overview of poke and lick behavior during correct and incorrect trials. The IOP was defined from the NPR up to the moment the rats had started licking in 95% of all trials. Even though a reward was only delivered in correct trials (and upon nose poke entry), rats initiated the lick response in all trials (rewarded and unrewarded) and adapted their licking behavior based on the presence of reward thereafter. Licking behavior thus typically consisted of initial licks to sample for reward delivery, followed by more licks for reward consumption in correct trials. b) Three example PER cells that differentiated between trial outcomes during the IOP, when rats sustained their nose poke to sample for reward delivery. c) As opposed to PER cells, 3 example cells from S1BF, V2L, and HPC are shown that became largely selective for trial outcome after the IOP, when lick and poke-exit behavior depended on the actual trial outcome ($t = 0$ marks the onset of the IOP; vertical dashed line marks the end of the IOP).

the delivery of reward itself, because the majority coded for the omission of reward (Fig. 10g; $Z = 3.285$, $P < 0.001$, proportion z-test: 18 error-up cells > 5 correct-up cells). These results indicate that, when rats start sampling for reward delivery, PER cells mainly signal negative outcome.

Because PER cells preferentially encoded the choice and outcome following the NPR, we compared the time course between choice side and trial outcome coefficients based on the GLM coefficients (Fig. 10h). Overlaid densities of preferential choice side and trial outcome encoding revealed that the PER simultaneously encoded the trial outcome and choice side in the IOP, when rats sampled for reward delivery. Together, these results suggest that the PER integrates choice information with feedback on reward. This contrasted to the 2 sensory regions and HPC for which correlates were more tied to epochs of self-motion, likely arising from corollary discharge and sensory input during locomotion or from spatial coding (such as place fields for hippocampal cells).

Discussion

In this study, we characterized the neural correlates of multisensory object sampling, choice side, and trial outcome at prominent processing stages of the cortico-hippocampal hierarchy by conducting quadruple-area ensemble recordings in rats performing a multisensory object recognition task.

Our first hypothesis regarding the PER, pertaining to its potential contribution to object perception for familiar objects, predicted that object sampling would lead to sensory responses in S1BF, V2L, and PER, and that the HPC would be less affected by the sensory modality at hand. Active touch evoked neural activity in S1BF and HPC, but not in V2L or PER. Light input at the start of visual sampling evoked neural responses in V2L and HPC, but not in S1BF or PER. Predominant responses to touch or light input were thus absent in PER, despite its known reciprocal anatomical connectivity to sensory cortical regions (Agster and Burwell 2009; Burwell et al. 1995). Importantly, PER was not systematically sampled along the full rostro-caudal axis. Tracing studies suggest that visual input mainly targets caudal PER, and tactile input primarily targets the rostral PER (Agster and Burwell 2009). Modality-specific sensory input might thus be restricted to small subregions of the PER and could therefore be missed when recording cell samples. The majority of our PER recordings was performed in central-to-caudal PER (Figs. 2a and S1), which has reciprocal projections with higher-order visual areas such as V2L but less so with S1BF (Agster and Burwell 2009). Absence of visual responses in PER is therefore all the more striking, as is the contrast to HPC and sensory regions given that PER is often considered to be a relay station between sensory cortices and the rest of the medial temporal lobe (MTL), including HPC (Naber et al. 1997; Doan et al. 2019; Fiorilli et al. 2021). Altogether, the present

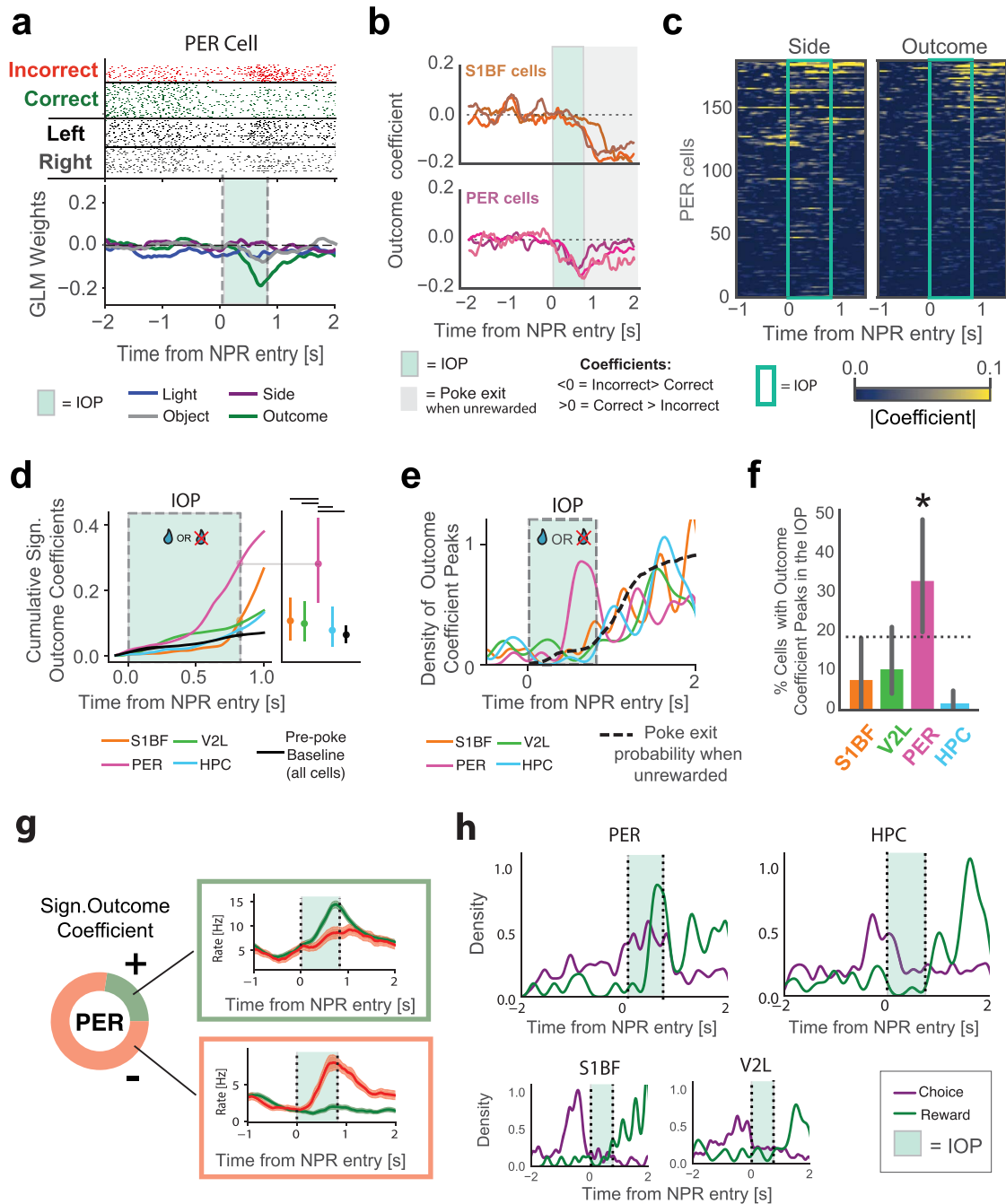


Fig. 10. Simultaneous encoding of choice side and unexpected outcome in PER. **a**) One example PER cell revealing negative GLM weights for the outcome. The negative outcome weights reflect the increased firing rate during an unrewarded IOP. Cyan area = IOP (as in **b**, **d**, **e**, **g**, and **h**). **b**) Outcome coefficient time course of 3 example S1BF (orange) and PER (magenta) cells. Note that the outcome coefficients in S1BF cells increased after the IOP and are therefore likely driven by nose poke exits upon reward omissions. PER cells encoded the outcome earlier, when holding the NPR during the IOP (shaded cyan area). **c**) Time course of coefficient magnitudes for choice side (left) and outcome (right) for all PER cells. Cells are ordered according to their maximum outcome coefficient magnitude. Highest outcome coefficient magnitudes in PER clustered toward the end of the IOP (cyan outline), whereas the choice side was often encoded already before the NPR. **d**) Left: time course of cumulative outcome modulation following reward port entry. Outcome modulation is quantified by the cumulative sum of outcome coefficient magnitudes over time, averaged over all cells from a given area. Only cells with a significant coefficient for the outcome at any time bin are included. Right: cumulative sum of outcome coefficient magnitude at the end of the IOP. Colored vertical bars are CIs, horizontal bar for significant comparisons ($P < 0.05$, 1-way ANOVA [$F = 8.385$, $P < 0.000$] with post hoc Tukey test). **e**) Time course of preferential trial outcome modulation for each area, based on the peak moment of the coefficient magnitude per significant cell. **f**) Percentage of significant cells that are modulated by outcome strongest during IOP as opposed to outside of the IOP (S1BF: 7.9%; V2L: 10.9%; PER: 30.3%; HPC: 1.6%). Bars are permutation-based CIs, * for significantly higher percentages than uniformly distributed events ($P < 0.05$, 1-sided z-test of proportions). **g**) Left side: proportions of significantly modulated PER cells having positive and negative outcome coefficients. Negative outcome coefficients resulted from higher firing rates during unrewarded IOPs compared with rewarded IOPs. Right side: example cells responding to reward delivery or reward omission. Green and red traces indicate firing rates during rewarded and unrewarded trials, respectively. **h**) Overlaid densities of poke-aligned times at which cells maximally differentiate between choice side (purple) and trial outcome (green), based on GLM coefficients. Only cells with significant coefficients for the given predictor (choice side or trial outcome) are included in the densities. Cells in the PER preferentially encoded both the choice side and the outcome (mainly reward omissions) when rats held the NPR during the IOP. The HPC and the sensory regions encoded outcome-related parameters after rats exited the reward site.

study supports the notion that sensory cortices are primarily modulated by their primary modality, and that multisensory (or amodal) processing is more abundant in the HPC compared with the PER and sensory regions considered here.

The object identity could be decoded from individual cells in V2L during visual sampling, but not during tactile sampling. Object identity was not prominently encoded by individual cells in the other regions during tactile sampling. Cells in S1BF may primarily represent low-level sensory features such as the angles and speed of whiskers upon object contact (Arabzadeh et al. 2004; Fassihi et al. 2020), much like cells in the primary visual system are mainly tuned by low-level visual features. Additionally, V2L represented the object through the collective activity of cell populations only in visual trials, whereas S1BF did so exclusively in tactile trials. An additional amodal population code for the objects emerged in the HPC later in time, throughout most of the ITI. This suggests a sustained object memory signal in the HPC initiated by reward-based feedback following the NPR. Altogether, these results show that representations of solid, 3D objects can exist in higher-order sensory cortex, as well as in the HPC without a robust object representation in PER—even though this subregion receives many afferent fibers from the sensory cortices and communicates with HPC (Agster and Burwell 2009). Aside from modality-specific responses, object sampling did not lead to prominent amodal “object fields” in PER, as described in large open field environments, where rats explored objects spontaneously (Burke et al. 2012). As previously proposed, the behavioral task may require a spatial-navigational component for spatial firing fields to arise in PER (Ahn and Lee 2015; Bos et al. 2017; Fiorilli et al. 2021). Notably, the objects we used were highly familiar to the rats and not explicitly configured to be ambiguous, which might be factors that lower the perceptual-mnemonic demands and recruitment of MTL structures such as PER (von Linstow et al. 2016; Doron et al. 2020). For instance, it is possible that sensory or invariant object representations only arise in PER when stimuli are novel, and this awaits future studies. Nonetheless, our results dispute an important, general perceptual-mnemonic role for PER in coding object-specific features when familiar objects are actively sampled and recognized.

PER and the neural coding of unexpected motivational outcome

The most prominent responses in PER were found after the animal's arrival at the reward sites. First, PER was the only region in which cells preferentially encoded the choice side just after the NPR, as opposed to during the choice phase (Fig. 8). Second, PER cells were responsive to the motivational outcome of a spatial choice during the reward delivery phase, just when rats started licking to sample for reward delivery. These signals were specific for the PER; correlates of trial outcome in HPC and the sensory neocortex were observed only when rats started to terminate the NPR (Figs. 9, 10c, and S5c). In PER, signaling of reward omission was more often observed than when reward was delivered. This may relate to the larger degree of surprise associated with omissions than deliveries, because the range of correct responses ranged between 70% and 85% of trial types in which objects were presented (Fig. 1d). A systematic variation of (both negative and positive) surprise in trial outcome, applied against a background of variable reward history, must await future investigations.

Because PER firing responses peaked after reward port entry (when the subject was immobile), these PER responses (reported as population responses and GLM coefficients) are unlikely to be driven by locomotion, vestibular-proprioceptive inputs, or by

differential sensory flow accompanying body movements toward reward ports. Even though PER cells coded for choice side most strongly after the arrival at a goal location, the PER started to differentiate between sides (but not between outcomes) already before arrival at the goal locations (Figs. 8c and d and 10h). This suggests that these cells anticipated the subject's arrival at a given goal location: the closer to a given reward goal, the higher the firing rates for a specific population of PER cells. The relevance of reward delivery for PER firing is supported by earlier work demonstrating that PER cells lock onto large spatial segments of a maze associated with reward- and other task-related events; these firing fields generally peak at, or close to, goal locations (Bos et al. 2017). However, in this earlier study, reward delivery was not accurately timed in relation to PER firing. Overrepresentation of motivationally relevant locations has been described in the HPC by the clustering of (usually small) place fields near reward sites (Hollup et al. 2001; Lansink et al. 2012; Gauthier and Tank 2018). The excess density of choice-side coding in HPC cells just before arrival at goal locations (Figs. 8d and S3b) aligns well with such overrepresentation. PER firing responses are notably distinct from place cells observed in HPC as they preferentially encode the choice side after the NPR, as opposed to place cells activated before or upon arrival at reward sites (Figs. 6c and 8d).

The observed neural correlates of outcome in PER are reminiscent of value and reward prediction signals in TDRL algorithms, neural correlates of which have been attributed to mesencephalic dopamine neurons (Mirenowicz and Schultz 1994, 1996; Schultz et al. 1997; Stalnaker et al. 2019; but see Rusu and Pennartz 2020). A single dopaminergic cell may encode both positive and negative prediction error, whereas PER cells in our study were found to code by way of reward-up or omission-up firing-rate responses. Recently, comparable reward value signals have been reported in the serotonin system, such as in the dorsal raphe nucleus, which is well connected to the PER (Vertes et al. 1999; Bromberg-Martin et al. 2010). Much like dopamine signals, sustained activity of dorsal raphe neurons can be driven by expected reward, and signal positive or negative reward prediction errors. In contrast to midbrain dopaminergic neurons which are phasically excited by positive errors and decrease firing activity upon negative errors, serotonergic neurons are primarily excited by punishment (Cohen et al. 2015). Encoding of punishment may be reminiscent of, but is different from signaling the omission of an expected reward, which is the predominant effect seen in PER neurons.

As compared with Ahn and Lee (2015) on rat PER, we already noted some similarities in findings, but several points can be highlighted where the current study goes significantly beyond their results. First, we recorded from 3 other cortical areas in addition to PER, which allowed us to establish a positive control for object coding as compared with the null finding, viz. that PER, somewhat surprisingly, does not code object identity. Our finding that V2L neurons did code object identity (Fig. 5) shows that the solid, 3D objects, and the task protocol we used were suitable for identifying object correlates in the neocortex, which was not shown by Ahn and Lee (2015), using 2D images as visual stimuli. Second, Ahn and Lee's task deployed an auditory cue, delivered at the time of the choice response in their task, to signal whether the rat's behavioral response was correct or not, which confounds the identification of choice correlates with both sensory input (tone) and tone-induced changes in reward expectation. Third, Ahn and Lee did not segregate the reward consumption phase from an earlier IOP period (as in Figs. 9 and 10), making it difficult to disentangle effects of reward from those of whole-body motor activity elicited by (non-)reward. These confounding factors may explain why these authors found relatively many PER cells to

be modulated during the behavioral choice phase and less cells whose activity could be specifically related to reward or its expectation.

In line with Eradath et al. (2015), one of the primary objectives of our study was to characterize the neural representations of stimuli and their corresponding reward outcomes in PER. Eradath et al. (2015) found that cells in PER of macaque monkeys represent cue-outcome associations and temporal context. PER cells mainly represented the outcome type contingent on the cue and showed sustained activity from cue onset until the next trial. This representation depended on visual stimuli and was not present when rewards were given independently of cues. A distinct feature of our study is the incorporation of multisensory stimuli, which provides a unique perspective on the encoding and representation of cue-outcome associations in real-world scenarios. Our results diverge from previous research by revealing that even with the inclusion of multisensory stimuli, clear object representations were not evident in the PER. This finding challenges the prevailing notion and suggests that other neural mechanisms or regions (i.e. V2L) may play a more prominent role in object perception.

The causal involvement of the rodent PER in object perception or memory has often been investigated by assessing impairments in detecting odd or novel items (Bartko et al. 2007; Albasser et al. 2015; Reid et al. 2012). In the context of reinforcement learning, novelty is frequently viewed as a predictor of a possible reward, or as being rewarding in and of itself, which encourages exploration before actual appetitive benefits are realized (Kakade and Dayan 2002; Akiti et al. 2022). The current study reports neural representations of rewarded locations (i.e. sites where the NPR is produced) co-occurring with reward-outcome signals in PER, suggesting that PER lesions might disrupt the assignment of error-signals to unexpected items associated with novelty detection.

It may thus be hypothesized that PER facilitates learning and adaptive behavior by taking part in signaling unexpected reward events (be it as negative or positive surprise) for specific actions such as spatial choices, wherein the interaction with serotonin and/or dopamine signaling needs further investigation. As elsewhere in the cortex, pyramidal cells of the PER use glutamate as neurotransmitter, and it is noteworthy that Reinforcement Learning based on deviations from expected reward can also be implemented in models using glutamatergic, Hebbian synapses (Pennartz 1997). The hypothesis that PER plays an important role in reward-dependent learning is supported by Doron et al. (2020) showing that PER outputs arriving in layer 1 of rodent somatosensory cortex are critical for learning associations between stimuli and reward. These associations become unnecessary for correct task performance once the task rule has been acquired.

Altogether, the present study challenges the notion that PER is generally involved in perceptual processing, suggesting that deficits in visually guided behavior observed after PER lesions may be primarily because of deficits in predicting reward outcomes and novelty detection. This interpretation is supported by the absence of such reward-based feedback in V2L, S1BF, and HPC. It further suggests that the final stage of visual object perception takes place upstream of PER (e.g. V2L or TeA), whereas the PER plays a critical role in learning and remembering associative relations among events but does not contribute significantly to object perception. This suggestion is in line with the relatively poor functional connectivity (as quantified by single neuron-to-population coupling) the rat PER displays toward sensory cortices and HPC in a visual discrimination task (Dorman et al. 2023). Further studies examining learning under parametric variations of reward parameters will be required to determine how motivational feedback and error signaling in the PER compare to adjacent

structures in the MTL, such as the postrhinal and entorhinal cortices. More work along these lines is needed to characterize the input-output wiring of reward-related cells in PER in more detail, and to quantify how signaling of unexpected outcomes and errors evolves over the course of learning.

Acknowledgments

The authors would like to thank Jeroen Bos and Laura Mourik Donga for their technical support for surgeries and hyperdrive assembly. We additionally thank Charlotte Oomens and Carien Lansink for their input and advice on the behavioral paradigm and training procedure. We are grateful for the support provided by the Technology Center of the University of Amsterdam, in particular by Sven Koot, Tristan van Klingeren, Gerrit Hardeman, Tjeerd Weijers, Udo van Hes, and Alix Wattjes. We thank C. Rossant, members of the Cortex Lab (UCL), and contributors for Klusta and Phy spike sorting software and the HBP data services for data curation.

Author contributions

Julien Fiorilli (Conceptualization, Data curation, Formal analysis, Investigation, Methodology, Project administration, Software, Visualization, Writing—original draft), Pietro Marchesi (Formal analysis, Software), Thijs Ruikes (Data curation, Software), Gerjan Huis in 't Veld (Methodology), Rhys Buckton (Methodology), Mariana D. Quintero (Investigation, Methodology), Ingrid Reiten (Data curation, Software), Jan G. Bjaalie (Data curation, Software), and Cyriel M.A. Pennartz (Conceptualization, Funding acquisition, Methodology, Supervision, Writing—review & editing)

Supplementary material

Supplementary material is available at *Cerebral Cortex* online.

Funding

This project has received funding from the European Union's Horizon 2020 Framework Programme for Research and Innovation under the Specific Grant Agreement No. 945539 (Human Brain Project SGA3) to C.M.A.P.

Conflict of interest statement. None declared.

Data availability

All relevant data are available from the authors, or from EBRAINS: <https://doi.org/10.25493/AM91-2D>.

References

- Agster KL, Burwell RD. Cortical efferents of the perirhinal, postrhinal, and entorhinal cortices of the rat. *Hippocampus*. 2009;19(12):1159–1186.
- Agster KL, Tomás Pereira I, Saddoris MP, Burwell RD. Subcortical connections of the perirhinal, postrhinal, and entorhinal cortices of the rat. II. Efferents. *Hippocampus*. 2016;26(9):1213–1230.
- Ahn JR, Lee I. Neural correlates of object-associated choice behavior in the perirhinal cortex of rats. *J Neurosci*. 2015;35(4):1692–1705.

- Akita K, Tsutsui-Kimura I, Xie Y, Mathis A, Markowitz JE, Anyoha R, Datta SR, Mathis MW, Uchida N, Watabe-Uchida M. Striatal dopamine explains novelty-induced behavioral dynamics and individual variability in threat prediction. *Neuron*. 2022:S0896-6273(22):00758–00759.
- Albasser MM, Olarte-Sánchez CM, Amin E, Brown MW, Kinnavane L, Aggleton JP. Perirhinal cortex lesions in rats: Novelty detection and sensitivity to interference. *Behav Neurosci*. 2015;129(3):227–43. <https://doi.org/10.1037/bne0000049>. PMID: 26030425; PMCID: PMC4450885.
- Alvarez P, Squire LR. Memory consolidation and the medial temporal lobe: a simple network model. *Proc Natl Acad Sci U S A*. 1994;91(15):7041–7045.
- Arabzadeh E, Panzeri S, Diamond ME. Whisker vibration information carried by rat barrel cortex neurons. *J Neurosci*. 2004;24(26):6011–6020.
- Bartko SJ, Winters BD, Cowell RA, Saksida LM, Bussey TJ. Perceptual functions of perirhinal cortex in rats: zero-delay object recognition and simultaneous oddity discriminations. *J Neurosci*. 2007;27(10):2548–2559.
- Berg RW, Kleinfeld D. Rhythmic whisking by rat: retraction as well as protraction of the vibrissae is under active muscular control. *J Neurophysiol*. 2003;89:104–117.
- Bernardi S, Benna MK, Rigotti M, Munuera J, Fusi S, Salzman CD. The geometry of abstraction in the hippocampus and prefrontal cortex. *Cell*. 2020;183(4):954–967.e21.
- Bjerke IE, Øvsthus M, Papp EA, Yates SC, Silvestri L, Fiorilli J, Pennartz CMA, Pavone FS, Puchades MA, Leergaard TB, et al. Data integration through brain atlasing: human brain project tools and strategies. *Eur Psychiatry*. 2018;50:70–76.
- Bos JJ, Vinck M, van Mourik-Donga LA, Jackson JC, Witter MP, Pennartz CMA. Perirhinal firing patterns are sustained across large spatial segments of the task environment. *Nat Commun*. 2017;8:15602.
- Bos JJ, Vinck M, Marchesi P, Keestra A, van Mourik-Donga LA, Jackson JC, Verschure PFMJ, Pennartz CMA. Multiplexing of information about self and others in hippocampal ensembles. *Cell Rep*. 2019;29(12):3859–3871.e6.
- Bromberg-Martin ES, Hikosaka O, Nakamura K. Coding of task reward value in the dorsal raphe nucleus. *J Neurosci*. 2010;30(18):6262–6272.
- Burke SN, Maurer AP, Hartzell AL, Nematollahi S, Uprety A, Wallace JL, Barnes CA. Representation of three-dimensional objects by the rat perirhinal cortex. *Hippocampus*. 2012;22:2032–2044.
- Burwell RD, Witter MP, Amaral DG. Perirhinal and postrhinal cortices of the rat: a review of the neuroanatomical literature and comparison with findings from the monkey brain. *Hippocampus*. 1995;5(5):390–408.
- Bussey TJ, Saksida LM. Object memory and perception in the medial temporal lobe: an alternative approach. *Curr Opin Neurobiol*. 2005;15(6):730–737.
- Cohen JY, Amoroso MW, Uchida N. Serotonergic neurons signal reward and punishment on multiple timescales. *eLife*. 2015;4:e06346.
- Deshmukh SS, Johnson JL, Knierim JJ. Perirhinal cortex represents nonspatial, but not spatial, information in rats foraging in the presence of objects: comparison with lateral entorhinal cortex. *Hippocampus*. 2012;22:2045–2058.
- Dickerson BC, Eichenbaum H. The episodic memory system: neurocircuitry and disorders. *Neuropsychopharmacology*. 2010;35(1):86–104.
- Doan TP, Lagartos-Donate MJ, Nilssen ES, Ohara S, Witter MP. Convergent projections from perirhinal and postrhinal cortices suggest a multisensory nature of lateral, but not medial. *Entorhinal Cortex Cell Rep*. 2019;29(3):617–627.e7.
- Dorman R, Bos JJ, Vinck MA, Marchesi P, Fiorilli J, Lorteije JAM, Reiten I, Bjaalie JG, Okun M, Pennartz CMA. Spike-based coupling between single neurons and populations across rat sensory cortices, perirhinal cortex, and hippocampus. *Cereb Cortex*. 2023;33(13):8247–8264.
- Doron G, Shin JN, Takahashi N, Drüke M, Bocklisch C, Skenderi S, de Mont L, Toumazou M, Ledderose J, Brecht M, et al. Perirhinal input to neocortical layer 1 controls learning. *Science*. 2020;370(6523):eaaz3136.
- Eichenbaum H. A cortical-hippocampal system for declarative memory. *Nat Rev Neurosci*. 2000;1:41–50.
- Eradath MK, Mogami T, Wang G, Tanaka K. Time context of cue-outcome associations represented by neurons in perirhinal cortex. *J Neurosci*. 2015;35(10):4350–4365.
- Fassihi A, Zuo Y, Diamond ME. Making sense of sensory evidence in the rat whisker system. *Curr Opin Neurobiol*. 2020;60:76–83.
- Fiorilli J, Bos JJ, Grande X, Lim J, Düzel E, Pennartz CMA. Reconciling the object and spatial processing views of the perirhinal cortex through task-relevant unitization. *Hippocampus*. 2021;31(7):737–755.
- Gauthier JL, Tank DW. A dedicated population for reward coding in the hippocampus. *Neuron*. 2018;99(1):179–193.e7.
- Glaser JJ, Benjamin AS, Chowdhury RH, Perich MG, Miller LE, Kording KP. Machine learning for neural decoding. *eNeuro*. 2020;7(4):ENEURO.0506-19.2020.
- Harris JA, Petersen RS, Diamond ME. Distribution of tactile learning and its neural basis. *Proc Natl Acad Sci U S A*. 1999;96(13):7587–7591.
- Hollup SA, Molden S, Donnett JG, Moser MB, Moser EI. Accumulation of hippocampal place fields at the goal location in an annular watermaze task. *J Neurosci*. 2001;21(5):1635–1644.
- Jacklin DL, Cloke JM, Potvin A, Garrett I, Winters BD. The dynamic multisensory engram: neural circuitry underlying crossmodal object recognition in rats changes with the nature of object experience. *J Neurosci*. 2016;36(4):1273–1289.
- Kajiwarra R, Takashima I, Mimura Y, Witter MP, Iijima T. Amygdala input promotes spread of excitatory neural activity from perirhinal cortex to the entorhinal-hippocampal circuit. *J Neurophysiol*. 2003;89(4):2176–2184.
- Kakade S, Dayan P. Dopamine: generalization and bonuses. *Neural Netw*. 2002;15(4–6):549–559.
- Lansink CS, Bakker M, Buster W, Lankelma J, van der Blom R, Westdorp R, Joosten RN, McNaughton BL, Pennartz CM. A split microdrive for simultaneous multi-electrode recordings from two brain areas in awake small animals. *J Neurosci Methods*. 2007;162(1–2):129–138.
- Lansink CS, Jackson JC, Ito R, Everitt BJ, Robbins TW, Pennartz CMA. Reward cues in space: commonalities and differences in neural coding by hippocampal and ventral striatal ensembles. *J Neurosci*. 2012;32(36):12444–12459.
- Liu Z, Richmond BJ. Response differences in monkey TE and perirhinal cortex: stimulus association related to reward schedules. *J Neurophysiol*. 2000;83(3):1677–1692.
- Mathis A, Mamidanna P, Cury KM, Abe T, Murthy VN, Mathis MW, Bethge M. DeepLabCut: markerless pose estimation of user-defined body parts with deep learning. *Nat Neurosci*. 2018;21(9):1281–1289.

- Mirenowicz J, Schultz W. Importance of unpredictability for reward responses in primate dopamine neurons. *J Neurophysiol*. 1994;72(2):1024–1027.
- Mirenowicz J, Schultz W. Preferential activation of midbrain dopamine neurons by appetitive rather than aversive stimuli. *Nature*. 1996;379(6564):449–451.
- Mitchinson B, Martin CJ, Grant RA, Prescott TJ. Feedback control in active sensing: rat exploratory whisking is modulated by environmental contact. *Proc R Soc Lond B*. 2007;274(1613):1035–1041.
- Murray EA, Bussey TJ. Perceptual-mnemonic functions of the perirhinal cortex. *Trends Cogn Sci*. 1999;3(4):142–151.
- Naber PA, Caballero-Bleda M, Jorritsma-Byham B, Witter MP. Parallel input to the hippocampal memory system through peri- and postrhinal cortices. *Neuroreport*. 1997;8(11):2617–2621.
- Norman G, Eacott MJ. Impaired object recognition with increasing levels of feature ambiguity in rats with perirhinal cortex lesions. *Behav Brain Res*. 2004;148(1–2):79–91.
- Papp EA, Leergaard TB, Calabrese E, Johnson GA, Bjaalie JG. Waxholm Space atlas of the Sprague Dawley rat brain. *Neuroimage*. 2014;97:374–86. <https://doi.org/10.1016/j.neuroimage.2014.04.001>.
- Pennartz CM. The ascending neuromodulatory systems in learning by reinforcement: comparing computational conjectures with experimental findings. *Brain Res Brain Res Rev*. 1995;21(3):219–245.
- Pennartz CM. Reinforcement learning by Hebbian synapses with adaptive thresholds. *Neuroscience*. 1997;81(2):303–319.
- Puchades MA, Csucs G, Ledergerber D, Leergaard TB, Bjaalie JG. Spatial registration of serial microscopic brain images to three-dimensional reference atlases with the QuickNII tool. *PLoS One*. 2019;14(5):e0216796. <https://doi.org/10.1371/journal.pone.0216796>.
- Reid JM, Jacklin DL, Winters BD. Crossmodal object recognition in rats with and without multimodal object pre-exposure: no effect of hippocampal lesions. *Neurobiol Learn Mem*. 2012;98(3):311–9. <https://doi.org/10.1016/j.nlm.2012.09.001>. Epub 2012 Sep 10. PMID: 22975081.
- Rolls BJ, Rowe EA. Exercise and the development and persistence of dietary obesity in male and female rats. *Physiol Behav*. 1979;23:241–247.
- Rossant C, Kadir SN, Goodman D, Schulman J, Hunter M, Saleem AB, Grosmark A, Belluscio M, Denfield GH, Ecker AS, et al. Spike sorting for large, dense electrode arrays. *Nat Neurosci*. 2016;19(4):634–641.
- Rusu S, Pennartz CMA. Learning, memory and consolidation mechanisms for behavioral control in hierarchically organized cortico-basal ganglia systems. *Hippocampus*. 2020;30(1):73–98.
- Sachdev RN, Berg RW, Champney G, Ebner F, Kleinfeld D. Unilateral vibrissa contact: changes in amplitude but not timing of rhythmic whisking. *Somatosens Mot Res*. 2003;20(2):163–169.
- Schultz W, Dayan P, Montague PR. A neural substrate of prediction and reward. *Science*. 1997;275(5306):1593–1599.
- Stalnaker TA, Howard JD, Takahashi YK, Gershman SJ, Kahnt T, Schoenbaum G. Dopamine neuron ensembles signal the content of sensory prediction errors. *eLife*. 2019;8:e49315.
- Sutton RS. Learning to predict by the methods of temporal differences. *Mach Learn*. 1988;3:9–44.
- Sutton RS, Barto AG. Toward a modern theory of adaptive networks – expectation and prediction. *Psychol Rev*. 1981;88:135–170.
- Vertes RP, Fortin WJ, Crane AM. Projections of the median raphe nucleus in the rat. *J Comp Neurol*. 1999;407(4):555–582.
- Vinck M, Bos JJ, Van Mourik-Donga LA, Oplaat KT, Klein GA, Jackson JC, Gentet LJ, Pennartz CM. Cell-type and state-dependent synchronization among rodent somatosensory, visual, perirhinal cortex, and hippocampus CA1. *Front Syst Neurosci*. 2016;9:187.
- von Linstow RE, Muller RU, Brown MW. Finding and not finding rat perirhinal neuronal responses to novelty. *Hippocampus*. 2016;26(8):1021–1032.